Principles governing the integration of landmark and self-motion cues in entorhinal cortical codes for navigation

Malcolm G. Campbell [1*], Samuel A. Ocko[2,3], Caitlin S. Mallory[1,3], Isabel I. C. Low[1], Surya Ganguli[1,2] and Lisa M. Giocomo [1*]

To guide navigation, the nervous system integrates multisensory self-motion and landmark information. We dissected how these inputs generate spatial representations by recording entorhinal grid, border and speed cells in mice navigating virtual environments. Manipulating the gain between the animal's locomotion and the visual scene revealed that border cells responded to landmark cues while grid and speed cells responded to combinations of locomotion, optic flow and landmark cues in a context-dependent manner, with optic flow becoming more influential when it was faster than expected. A network model explained these results by revealing a phase transition between two regimes in which grid cells remain coherent with or break away from the landmark reference frame. Moreover, during path-integration-based navigation, mice estimated their position following principles predicted by our recordings. Together, these results provide a theoretical framework for understanding how landmark and self-motion cues combine during navigation to generate spatial representations and guide behavior.

To navigate, the brain combines self-motion information with sensory landmarks to form a position estimate. The neural substrates thought to support such position coding include functionally defined medial entorhinal cortex (MEC) cell types[1], namely grid cells[2], head direction cells[3,4], border cells[5,6] and speed cells[7,8]. Together, these neurons generate an internal map of space, with their codes emerging from interactions between self-motion cues, such as locomotion and optic flow, and sensory cues from environmental landmarks.

However, the principles by which MEC cells integrate self-motion versus landmark cues remain incompletely understood. While several works indicate that grid cell patterns rely on self-motion cues[2,9–11], increasing evidence suggests that grid patterns emerge from a complex interaction between self-motion and sensory landmarks. For example, grid cells deform when the geometry of the environment changes, depend on environmental boundaries to maintain an error-free spatial map, and destabilize after visual landmarks are removed[2,12–19]. How multisensory self-motion cues combine to drive MEC speed cells remains equally unknown. Speed cells retain speed tuning in darkness, but firing rates decrease[16], suggesting that visual inputs calibrate their response. In addition, while previous works often ascribe the neural basis of path integration to MEC functionally defined cell types[1,2,9], the degree to which behaviorally measured path integration position estimates and MEC neural codes follow the same cue combination principles remains unclear[13–17].

Here we examine the principles by which both mouse behavior and MEC cell classes integrate self-motion with visual landmark cues (Fig. 1a). To do this, we analyzed the neural activity and behavior of mice while they explored virtual reality (VR) environments[20,21]. By combining these experimental approaches with an attractor-based network model, we propose a framework for understanding how optic flow, locomotion and landmark cues interact to generate MEC firing patterns and behavioral position estimates during navigation.

Results

We recorded MEC neural activity in 21 mice as they navigated unidirectional VR linear tracks for water rewards (Fig. 1b–d and Supplementary Figs. 1 and 2). Spatially responsive cells were classified on the basis of their tuning in an open field (grid $n = 151$ of 1,136, border $n = 160$ of 1,136; Methods) and identified in VR by matching waveforms (781 of 1,136 cells; 96 of 151 grid cells; 97 of 160 border cells; Fig. 1b,c and Supplementary Fig. 3). Many cells had spatially stable firing fields in VR, with VR stability values similar to those observed on a real-world linear track[22] (mean stability ± s.d.: grid, 0.40 ± 0.24; border, 0.54 ± 0.23; Fig. 1e,f and Supplementary Fig. 4). In VR, border cells were more stable than grid cells (Wilcoxon rank-sum $P = 4.4 \times 10^{-5}$), and the firing rate of border cells peaked near visual landmarks (repeated-measures ANOVA $P = 0.016$; Fig. 1e and Methods). In contrast, grid cell firing rates were more uniformly distributed across the track (repeated-measures ANOVA $P = 0.18$; Fig. 1e). This suggests that grid and border cells are driven by different cues in VR, with border cell firing likely determined by the locations of landmarks. We next investigated this further by manipulating the virtual environment.

To ascertain the contribution of locomotion versus visual cues (optic flow and visual landmarks) to the firing patterns of MEC neurons, we put these cues into conflict by altering the gain of the transformation between the rotation of the ball and translation of the VR track (Fig. 2)[21]. Manipulations followed an A–B–A′ design, with gain in B decreasing (0.5×) or increasing (1.5×) the visual scene translation (Fig. 2a). To avoid plasticity in the representation of the virtual environment, we limited the number of gain manipulation trials for each session (5 for gain decrease; 10 for gain increase). Grid cell (total $n = 80$, gain decrease $n = 65$, gain increase $n = 56$) and border cell (total $n = 68$, gain decrease $n = 44$, gain increase $n = 48$) firing patterns were analyzed with respect to virtual position on the track (Fig. 2b–d and Supplementary Fig. 5).

[1]Department of Neurobiology, Stanford University School of Medicine, Stanford, CA, USA. [2]Department of Applied Physics, Stanford University, Stanford, CA, USA. [3]These authors contributed equally:Samuel A. Ocko, Caitlin S. Mallory. *e-mail: malcolmc@stanford.edu; giocomo@stanford.edu
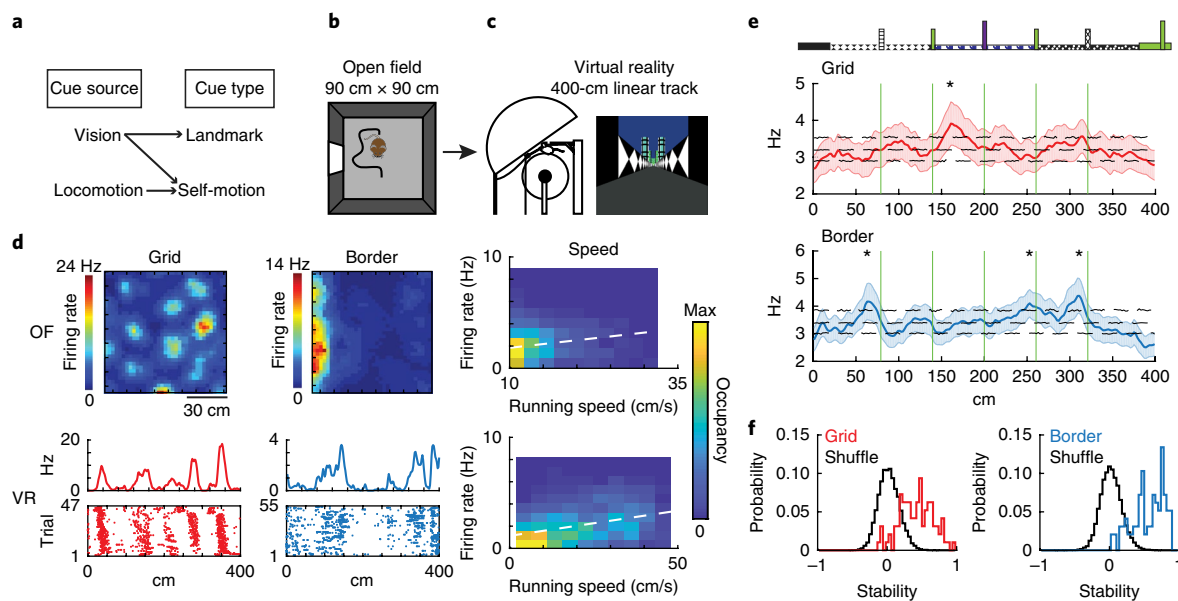
Fig. 1 | Functionally identified MEC cell types in real and virtual environments. a, Schematic of cue sources and types in VR. Cues can come from visual or locomotor input (cue source). Visual cues can provide information regarding visual landmarks (cue type) or self-motion in the form of optic flow (cue type). Locomotor cues also provide information regarding self-motion (cue type). **b**, The open field (OF) environment was a 90 × 90 cm square box with a single polarizing cue card. **c**, Following OF recordings, mice were immediately transferred to the VR setup. **d**, Example grid, border and speed cells recorded in OF (top row) and VR (bottom row). Grid and border cell VR data show firing rate (top) and spikes over trials (raster plots, bottom). Speed-cell data are plotted as a heat map of instantaneous firing rate with respect to running speed, with colors indicating the percentage of time bins with the corresponding firing rate and running speed. **e**, Average grid-cell firing rate (top) and border-cell firing rate (bottom) as a function of track location in baseline VR sessions. Only cells with stability >0.2 were analyzed ($n = 85$ grid cells, 87 border cells). Shaded regions show mean ± s.e.m. Vertical green lines show the locations of landmarks, and horizontal dashed black lines show the 5th, 50th and 95th percentiles of a shuffled distribution of firing rates. Asterisks indicate firing rate peaks that exceeded the 95th percentile of the shuffled distribution. **f**, Grid and border cells had significantly higher stability than shuffled distributions on the VR track ($P < 1 \times 10^{-30}$, $n = 96$ grid cells, 97 border cells, Wilcoxon rank-sum tests).

We considered three possible response types to altered gain: that the spatial firing pattern might degenerate, coherently remap or remain unchanged (Fig. 2c).

Grid and border cells retain stable patterns during gain manipulations. We first examined whether the spatial firing patterns of grid or border cells degenerated during gain manipulations. We quantified degeneration by computing the spatial stability within matched numbers of A- and B-period trials (Methods). Grid and border cell stability did not significantly decrease from the A to B period, except for grid gain increase sessions, in which stability decreased but was comparable to B-period values observed during all other gain sessions (Fig. 3a). Mean firing rates did not change (Supplementary Fig. 6a). To quantify structured changes in firing rate maps during gain manipulations, we next identified cells that remained stable (stability > 0.2 in both A and B), a criterion that was satisfied by the majority of grid and border cells (Fig. 3a and Supplementary Fig. 7a). For subsequent analyses of structured changes in firing patterns, only stable trial blocks were used.

Gain changes cause coherent remapping in grid cells but little change in border cells. Next we analyzed whether stable grid and border cell firing patterns change during gain manipulations by computing spatially lagged cross-correlations between A- and B-period rate maps (Fig. 3b). This cross-correlation measure discriminates among the possibilities shown in Fig. 2c. For example, a large cross-correlation peak at zero spatial lag indicates firing patterns do not change between baseline and a gain manipulation. This would be expected if grid or border cells were driven by visual cues, thereby locking their firing patterns to position on the virtual

track, regardless of any change in gain. Alternatively, a large peak at a nonzero spatial lag indicates coherent remapping in which firing patterns systematically shift due to a gain change. Finally, the lack of a large peak indicates a more complex remapping. For cells with multiple stable gain manipulation responses, correlations were averaged across manipulations.

For adjacent blocks of 5 trials within baseline, grid and border cells had high cross-correlations centered around zero spatial lag, confirming that these cells had spatially stable patterns in the baseline condition (correlation ± s.e.m.: grid gain decrease (33), 0.54 ± 0.03; border gain decrease (28), 0.60 ± 0.03; grid gain increase (37), 0.56 ± 0.02; border gain increase (30), 0.61 ± 0.03; Fig. 3b). Grid cells remapped during both gain decreases and increases, as indicated by the low A–B cross-correlations at zero lag (correlation ± s.e.m.: gain decrease, 0.07 ± 0.03; Wilcoxon test versus baseline $P = 9.4 \times 10^{-7}$; gain increase = 0.17 ± 0.03, Wilcoxon test versus baseline $P = 1.7 \times 10^{-7}$; Fig. 3b). In contrast, border cells remained remarkably stable during gain increases, but partially remapped during gain decreases (correlation ± s.e.m.: gain decrease, 0.34 ± 0.05; Wilcoxon test versus baseline $P = 0.00022$; gain increase, 0.54 ± 0.04; Wilcoxon test versus baseline $P = 0.16$; Fig. 3b). Even during gain decreases, however, border cells had significantly higher A–B correlations at zero lag than grid cells (Wilcoxon rank-sum test versus grid cells, gain decrease $P = 7.8 \times 10^{-5}$; gain increase $P = 4.0 \times 10^{-8}$; Fig. 3b). These data demonstrate that while grid and border cells had similar baseline stability, grid cells remapped during gain manipulations, whereas border cells primarily remained locked to the visual cues.

Grid cells respond asymmetrically to gain increases and decreases. We then characterized the nature of grid cell remapping
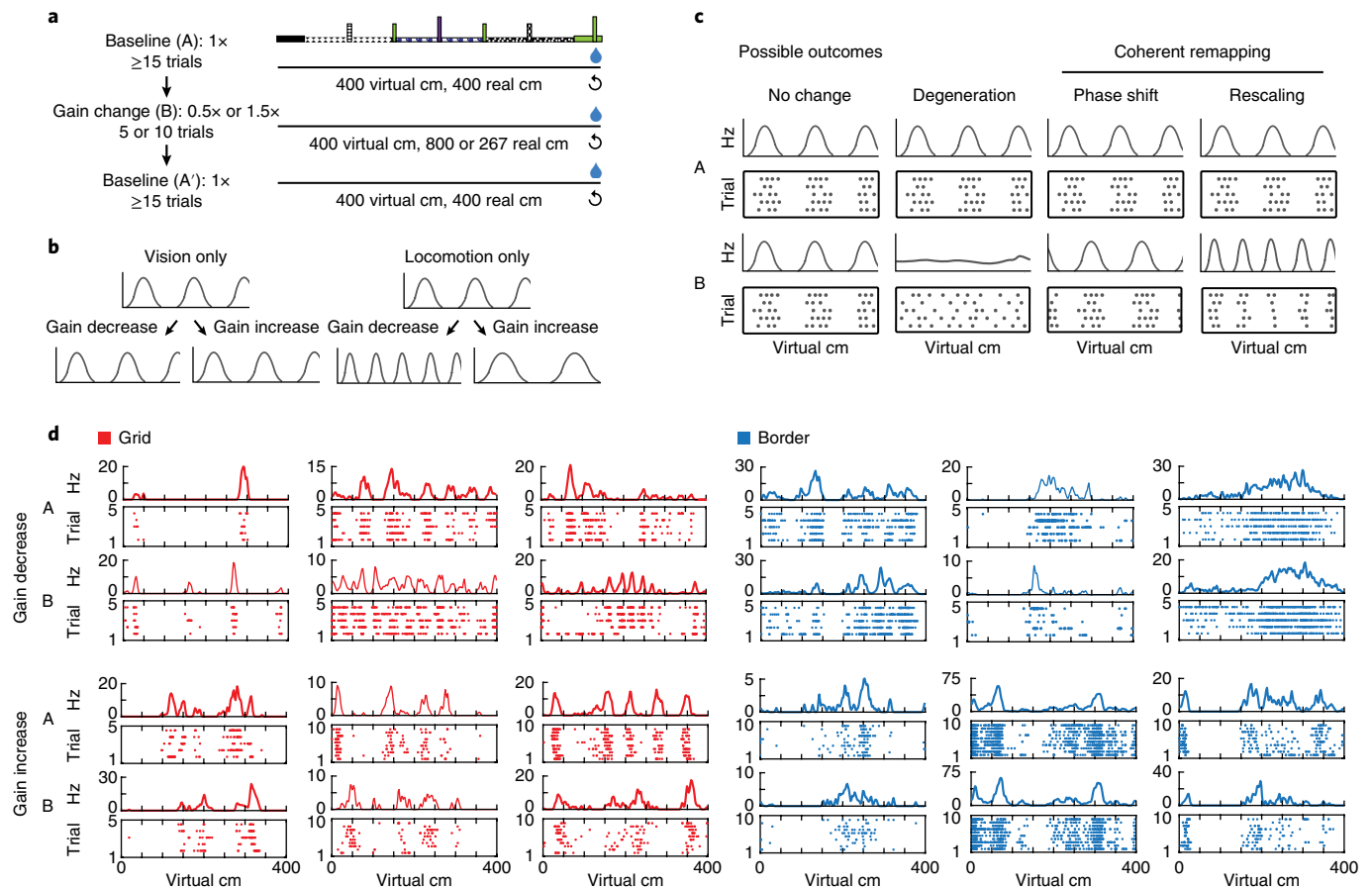
Fig. 2 | Gain manipulations place visual and locomotor cues in conflict. a, Experimental design. Mice ran ≥15 trials of baseline gain (A period) followed by 5 or 10 trials of gain decrease or gain increase (0.5× or 1.5×; B period). Gain decrease changed the real distance the animal had to run to reach the end of the track from 400 cm to 800 cm; gain increase changed this distance to 267 cm. Following the gain change period, mice ran a second baseline period of ≥15 trials (A′ period). **b**, Illustration showing two potential responses of grid or border cells to gain manipulations, with firing patterns plotted with respect to virtual position on the track. If the spatial firing pattern reflects only the influence of visual cues, no change in the spatial pattern would be observed during gain changes. If the spatial firing pattern reflects only the influence of locomotor cues, the frequency of the spatial pattern would increase in gain decreases and decrease in gain increases. **c**, We considered the following possible response types to gain manipulations: no change, degeneration, phase shift and rescaling. The last two are subtypes of coherent remapping. **d**, Example grid cell (left) and border cell (right) responses during baseline (A, top and bottom row), gain decrease (B, top row) and gain increase (B, bottom row).

during gain manipulations. For gain increases, a large peak in the A–B cross-correlation occurred at +12 cm, indicating a shift of the rate map forward along the track by this amount (correlation ± s.e.m.: 0.30 ± 0.04, $n = 37$; Fig. 3b). Cross-correlation peaks for individual cells were similar in magnitude between gain change and baseline, but shifted by varying amounts, resulting in a lower mean peak (peak correlation ± s.e.m.: baseline, 0.58 ± 0.02; gain change, 0.52 ± 0.03; $P = 0.14$; shift ± s.e.m.: baseline, −1.7 ± 0.5 cm; gain change, 14.4 ± 7.1 cm; $P = 0.0099$, Wilcoxon tests; Fig. 3b, bottom). For gain decreases, a smaller but still nonzero peak in the average A–B cross-correlation curve was present at −6 cm (correlation ± s.e.m.: 0.10 ± 0.03, $n = 33$; Wilcoxon test versus zero, $P = 0.0089$; Wilcoxon test gain decrease versus gain increase peak, $P = 0.00057$; Fig. 3b). Unlike for gain increases, the peaks of individual grid cells' A–B cross-correlations were smaller during gain decrease compared to baseline but were not shifted backward (peak correlation ± s.e.m.: baseline, 0.57 ± 0.02; gain change, 0.37 ± 0.03; $P = 1.4 \times 10^{-5}$; mean cross-correlation shift ± s.e.m.: baseline, −2.2 ± 0.5 cm; gain change, 16.5 ± 9.2 cm; $P = 0.050$; Wilcoxon tests; Fig. 3b, bottom). These results indicate that grid cells retained a coherent, but shifted, rate map during gain increases but not gain decreases. In contrast, some border cells shifted backward during

gain decreases, whereas others were stable (shift ± s.e.m.: baseline, −0.3 ± 0.9 cm; gain change, −27.4 ± 7.1 cm; Wilcoxon $P = 0.00086$), leading to an average A–B cross-correlation that peaked near zero (−2 cm) but with a leftward skew (Fig. 3b). Practically all border cells remained highly stable, with minimal shifts during gain increases (for shift, $P = 0.16$; for change in peak, $P = 0.94$; Wilcoxon tests, Fig. 3b).

Next we asked whether grid cells rescale during gain changes. The degree of rescaling can provide insight into the relative weighting of visual and motor speed input for grid cell path integration calculations, with larger degrees of rescaling indicating a larger influence of motor speed cues. For example, if motor cues are the primary input determining grid firing patterns, we should see a decrease in the grid spatial scale with respect to virtual position that matches the degree of gain decrease (Fig. 2b). To test this, we computed average autocorrelations of the rate maps in the A and B periods (Fig. 3c, top). We then contracted or expanded the A-period autocorrelogram and correlated this rescaled map with the B-period autocorrelogram (Fig. 3c, bottom). For gain decreases, these maps maximally overlapped when the baseline was scaled by a factor of 0.61, indicating that the field size of grid firing patterns decreased and rescaled by 78% (100% corresponds to a factor of 0.5; mean ± s.e.m. over

a

Grid, gain decrease (0.5×)
41 gain manipulations from 33 cells

Border, gain decrease (0.5×)
30 gain manipulations from 28 cells

Grid, gain increase (1.5×)
47 gain manipulations from 37 cells

Border, gain increase (1.5×)
31 gain manipulations from 30 cells

b

n = 33 stable grid cells, gain decrease

n = 28 stable border cells, gain decrease

n = 37 stable grid cells, gain increase
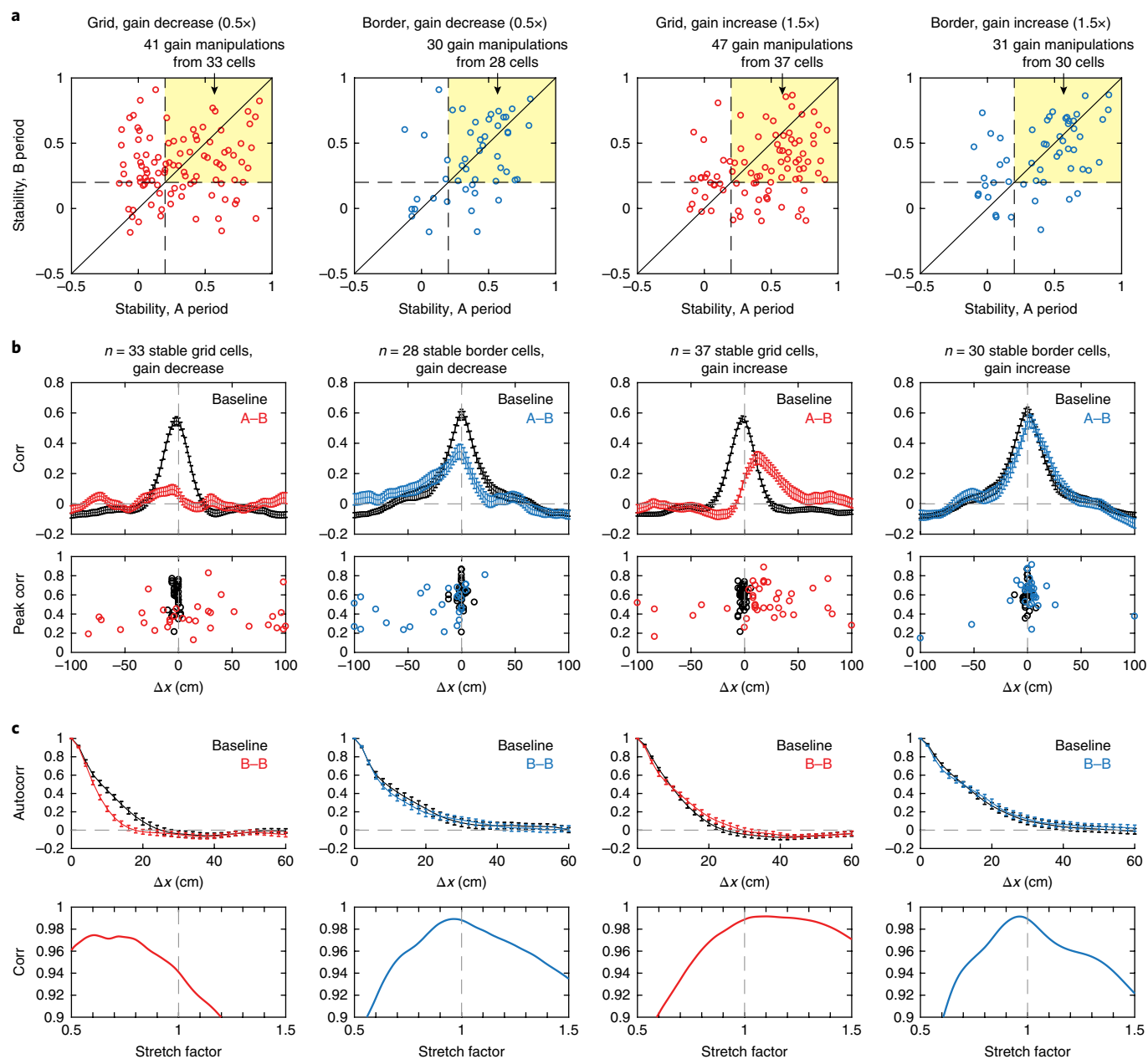
n = 30 stable border cells, gain increase

c

Fig. 3 | Structural analyses of gain change responses reveal an asymmetry in the weighting of visual and locomotor cues by grid cells. a, To analyze degeneration, we compared stability between the A period and B period. Except for grid gain increase, which had high baseline stability, stability did not decrease from the A period to the B period (stability ± s.d.: grid gain decrease A, 0.32 ± 0.30; B = 0.32 ± 0.24; $n = 98$ gain manipulations from 65 cells, $P = 0.83$; border gain decrease A, 0.39 ± 0.25; B, 0.38 ± 0.29; $n = 48$ gain manipulations from 44 cells, $P = 0.89$; grid gain increase A, 0.43 ± 0.29; B, 0.31 ± 0.24; $n = 88$ manipulations from 56 cells, $P = 0.00047$; border gain increase A, 0.41 ± 0.29; B, 0.40 ± 0.26; $n = 53$ gain manipulations from 48 cells, $P = 0.88$; Wilcoxon tests), indicating that degeneration was minimal. Only gain manipulations in which rate maps had stability > 0.2 in both the A period and B period (top right quadrant) were kept for further analysis (no. of cells with ≥ 1 stable trial block/no. of cells: grid gain decrease, 33/65; gain increase, 37/56; border gain decrease, 28/44; gain increase, 30/48). Each data point represents a single gain manipulation. Sometimes multiple gain manipulations were run for a single cell, in which case statistics such as cross- and auto-correlations were averaged by cell over all stable gain manipulations. **b**, Top: cross-correlations (corr) of firing rate maps. Baseline traces (black) show the average cross-correlation between adjacent blocks of 5 baseline trials that were both stable (stability > 0.2). Colored traces (red for grid cells, blue for border cells) show the cross-correlation between the A period (baseline trials immediately preceding gain change) and the B period (gain change). Grid cells responded differently to gain decreases and increases, showing a pronounced phase shift in gain increases but near complete remapping in gain decreases. Bottom: peak A–B cross-correlation versus location of peak for all cells individually. **c**, Top: average autocorrelations in the A and B periods for grid and border cells in gain decrease and gain increase revealed rescaling in grid cells during gain decreases. Bottom: to estimate the amount of rescaling, we stretched baseline autocorrelograms and correlated them with gain change autocorrelograms. Error bars: mean ± s.e.m.

individual cells, 54 ± 13%; Fig. 3c). Importantly, these scale changes were not a rescaling of the original firing pattern, but reflected new maps with smaller grid scales (Supplementary Fig. 6g,h). For gain

increases, the maximum was obtained at a scale factor of 1.10, indicating that the field size of grid firing patterns increased and rescaled by 20% (100% corresponds to a factor of 1.5; mean ± s.e.m.

over individual cells, $12 \pm 12\%$; Fig. 3c), significantly less than in gain decrease (Wilcoxon rank-sum $P = 0.016$). Border cells showed minimal rescaling in both manipulations (gain decrease scaling factor $= 0.96$, 8%; gain increase scaling factor $= 0.96$, −8%; Fig. 3c).

These rescaling results did not reflect rate map instability, as they were qualitatively identical when examining only the most stable cells (Supplementary Fig. 7). Moreover, within-trial autocorrelations, which are not affected by firing pattern drift across trials, showed similar results (Supplementary Fig. 7), as did changes in the number and size of firing fields (Supplementary Fig. 6). Grid cell responses were relatively uniform across the environment (Supplementary Fig. 8). Taken together, these analyses revealed that grid cells responded differently to gain increases and decreases: shifting in gain increases, with an occasional loss of fields (Supplementary Figs. 5 and 6e), and remapping and rescaling in gain decreases.

What mechanism might drive the grid rescaling we observed during gain manipulations? If grid cells estimate position using self-motion, then grid spacing should be inversely proportional to the magnitude of the velocity input to grid cells. In our experiments, this velocity input reflects a combination of locomotor and optic flow cues. The observed grid rescaling of 78% in gain decrease but only 20% in gain increase suggests that locomotor inputs exert a greater influence on grid cells in gain decrease. We next sought to investigate possible sources of this asymmetry by examining MEC speed signals during gain manipulations.

Multiple MEC speed signals respond asymmetrically to gain increases and decreases. In MEC, speed cells[7,8,23] and theta oscillations[7,24] carry information about running speed. We first analyzed speed cells, which could provide input to grid cells[8]. As the mouse's real running speed did not change during gain manipulations, we analyzed speed cells with respect to real running speed on the ball; in the previous section, grid and border cells were analyzed with respect to virtual position on the track. Thus, for these analyses, if locomotor cues are the primary input determining speed cell responses, the slope of firing rate as a function of speed should remain constant between baseline and gain conditions. If visual cues are the primary input determining speed cell responses, speed cell slope should increase with gain increases and decrease with gain decreases (Fig. 4a).

Speed cells were identified based on open field and VR recordings ($n = 33$ gain decrease, 41 gain increase; Fig. 4b,c and Supplementary Fig. 9; Methods). The mean firing rate of speed cells during running (speed > 2 cm/s) significantly increased in gain increases but did not change in gain decreases, suggesting that like grid cells, speed cells respond asymmetrically to gain manipulations (firing rate (Hz) $\pm$ s.e.m.: gain decrease A, 9.65 ± 1.63; B, 10.21 ± 1.71; Wilcoxon $P = 0.16$; gain increase A, 10.83 ± 1.51; B, 13.31 ± 1.96; Wilcoxon $P = 7.1 \times 10^{-5}$). To explore this further, we estimated the instantaneous firing rate by smoothing vectors of spike counts across time bins (~16.7 ms) and then linearly regressed instantaneous firing rate against running speed for each speed cell individually. Linear regression slopes significantly increased in gain increase but did not change in gain decrease (slope (cm⁻¹) $\pm$ s.e.m.: gain decrease A, 0.095 ± 0.014; B, 0.085 ± 0.013; Wilcoxon $P = 0.17$; gain increase A, 0.115 ± 0.016; B, 0.142 ± 0.020; Wilcoxon $P = 0.0013$; Fig. 4c,e). Intercepts of the linear fits did not change in either case (Fig. 4c,e and Supplementary Fig. 10). To estimate the percent weighting of visual cues by speed cells during gain changes, we converted plots of B-period slope versus A-period slope into polar coordinates and computed the average angle of the response (Fig. 4f). This method is robust to the overinfluence of speed cells with large slopes. Here full locomotor weighting corresponds to an angle of 45° and full visual weighting corresponds to arctan(0.5), or 26.6°, in gain decrease and arctan(1.5), or 56.3°, in gain increase. Angles were not

significantly different from 45° during gain decrease but were significantly larger than 45° during gain increase (mean $\pm$ s.e.m.: gain decrease, $42.8 \pm 2.2°$, $P = 0.37$; gain increase, $51.0 \pm 1.6°$, $P = 0.0011$; Wilcoxon test versus 45°; Fig. 4g,h). Expressed as a percentage, speed cell visual weights were larger during gain increase than gain decrease (mean $\pm$ s.e.m.: gain decrease, $11.9 \pm 12.0\%$; gain increase, $52.9 \pm 13.8\%$; Wilcoxon test $P = 0.0503$; Fig. 4i). Together, these findings show that, as a population, speed cells weighed visual cues more highly in gain increase than in gain decrease, mirroring the asymmetry found in grid cells.

Another MEC signal that is modulated by running speed is theta frequency of the local field potential[24,25]. We found that peak theta frequency was significantly higher in gain increase compared to baseline, but did not change in gain decrease (Supplementary Fig. 11a). Moreover, we found that the slope of theta frequency with respect to running speed significantly changed in gain increase but not gain decrease (Supplementary Fig. 11b,c). These results show that visual cues affect local field potential theta in MEC more for gain increases than decreases, paralleling the asymmetric effect of visual cues on speed cells during gain manipulations.

A coupled-oscillator attractor network model elucidates principles for the integration of landmarks and self-motion. Combined, our data point to an asymmetry in the integration of locomotion and visual cues by grid and speed cells during gain changes. What underlying principles govern this cue-integration process? Previous work has shown that grid cells rely on self-motion input[10], which can reflect locomotion and optic flow cues, as well as an error-correcting signal provided by landmarks[12]. However, gain changes alter the relationship between distance traveled and the locations of landmarks, as well as the relationship between locomotion and optic flow. Therefore, the responses observed in our data likely reflect a complex interaction between the effects gain changes have on these different relationships. To better understand these dynamics, we modeled the integration of self-motion with landmark input in a 1D attractor network (Fig. 5).

We added external landmark inputs to standard attractor-based path integration machinery, in which grid cells are modeled as a 1D periodic network of neurons with short-range excitatory and long-range inhibitory synaptic weight profiles (Fig. 5a and Supplementary Math Note)[26–29]. In the absence of external input, this neural architecture yields a family of steady-state bump activity patterns, in which grid cell responses are generated when the animal's velocity is used to drive phase advance in the network[27,30]. External landmark inputs drive neuronal activity that changes as a function of the animal's position relative to landmark cues and serve to reinforce the phase of the attractor network (Fig. 5b,c)[12,26]. In this framework, gain changes correspond to a mismatch between the phase, or position estimate, of the attractor network (red arrow, Fig. 5a,c) and the phase of the landmark input (blue arrow, Fig. 5b,c). In this situation, landmark inputs exert a corrective force on the attractor phase, pulling it toward the landmark phase (Fig. 5d). The dynamics governing this process are analogous to a coupled-oscillator system, in which the two oscillators are grid cells, described by the attractor phase, and landmark inputs, described by the landmark phase. Coupled-oscillator systems are well studied in physics[31] and provide a clarifying analogy for the cue-integration process here.

In the model, gain manipulations lead to two response types depending on how much path integration and landmark inputs disagree. In the 'subcritical' regime, when the two disagree by a small amount, landmark inputs continuously correct the evolving phase of the attractor network and force it to keep pace with the landmarks, albeit at a constant phase difference (Fig. 5e,f). In this situation, an equilibrium is reached wherein the grid pattern shifts, but does not change in scale. By contrast, in the 'supercritical' regime, when path integration and landmarks disagree by a large amount, the phase
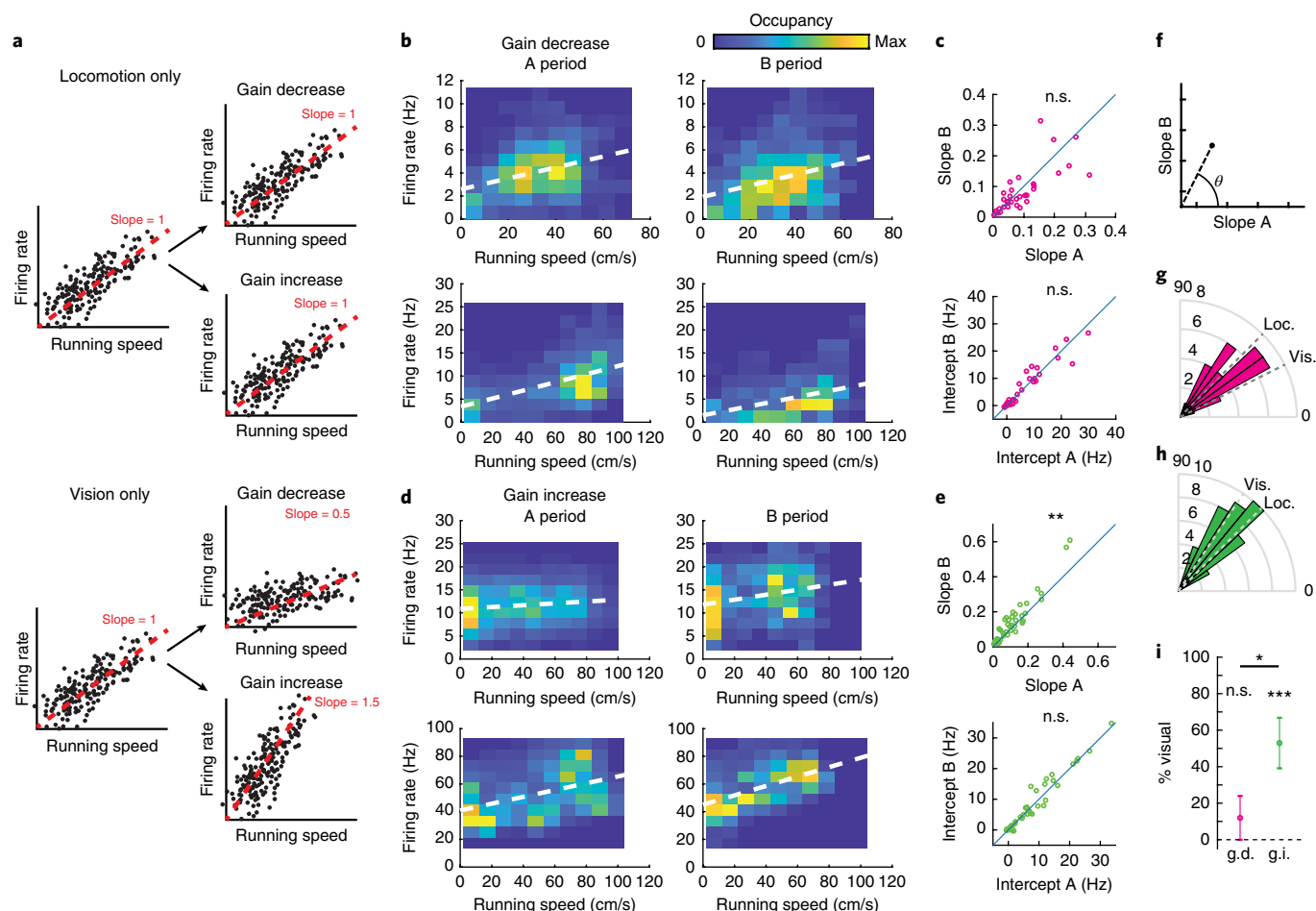
Fig. 4 | Gain-dependent integration of visual and locomotor cues by speed cells. a, Illustration showing two potential responses of speed cells to gain manipulations, with firing patterns plotted with respect to real running speed on the track. If the speed slope (firing rate versus running speed) reflects only the influence of locomotor cues, no change in the slope would be observed during gain changes. If the speed slope reflects only the influence of visual cues, the speed slope would decrease in gain decreases and increase in gain increases. **b**, Two example speed cell responses to gain decrease. Heat maps show instantaneous firing rate versus running speed, with colors indicating occupancy over time bins. White dashed lines show least-squares linear fits to data. **c**, Slope and intercept of linear fits did not significantly change for speed cells during gain decrease ($n = 33$; $P = 0.17$ slopes, $P = 0.99$ intercepts, Wilcoxon tests). **d,e**, Same as **b,c**, but for gain increase. In contrast to gain decrease experiments, slope of linear fit increased during gain increase ($n = 41$; $P = 0.0013$, Wilcoxon test). Intercepts did not change ($P = 0.79$, Wilcoxon test). **f**, Schematic showing the angle of a speed cell response to gain manipulation, based on the slope of the linear fit in the A period and the B period. The response of an individual neuron is illustrated as a black dot and the angle measured as θ. **g**, Distribution of angles for speed cells during gain decrease. Dotted lines show locomotion (loc.) response (45°) and visual (vis.) response (26.6°). **h**, Same as **f**, but for gain increase. Dotted lines show locomotion response (45°) and visual response (56.3°). **i**, Angles from **f** and **g** converted to percentages. Visual weights were higher during gain increase (g.i., green) than gain decrease (g.d., pink) ($n = 33$ g.d., 41 g.i.; $P = 0.0503$, Wilcoxon rank-sum test). Error bars: mean ± s.e.m. * $P = 0.0503$, ** $P < 0.01$, *** $P < 0.001$.

advance of the attractor network due to path integration breaks free from the landmark inputs. A consequence of this freedom, or decoherence, is that grid firing patterns remap and rescale (Fig. 5e,g). We derived a decoherence number D that demarcates the subcritical and supercritical regimes (Supplementary Math Note):

$$D = \frac{(k_A - k_L) \cdot v}{\omega}$$

The subcritical regime corresponds to $-1 < D < 1$. Outside this range, responses are supercritical. Here, $k_A - k_L$ is the degree of mismatch between the velocity-driven attractor advance and landmark inputs, v is the running speed of the mouse (assumed to be constant in the model), and ω is the strength of the landmark input. These three variables determine whether the response will be sub- or supercritical. Importantly, k_A corresponds to the self-motion input received by the attractor network. This does not need to be linear

with respect to VR gain, if the percentage weighting of locomotor versus visual speed cues changes with VR gain. In this way, we have derived a quantitative framework for understanding the interactions between velocity signals, path integration and landmarks in MEC codes.

Strikingly, our grid cell gain decrease data resembled the model's supercritical regime, and gain increase data resembled the subcritical regime (Fig. 3b,c versus Fig. 5f,g). The model's supercritical regime also explains the small bump in the cross-correlation during gain decreases (Fig. 3b) and the partial rescaling (Figs. 3c and 5g). What could drive this asymmetry in regimes across the two gain changes? We can combine our model with experimental measurements to answer this question. First, the mouse's running speed (v) was not different between baseline and either gain change (Supplementary Fig. 2), leaving landmark strength (ω) and velocity input (k_A) as candidate sources of the asymmetry. While the possibility remains that the partial remapping of border cells we
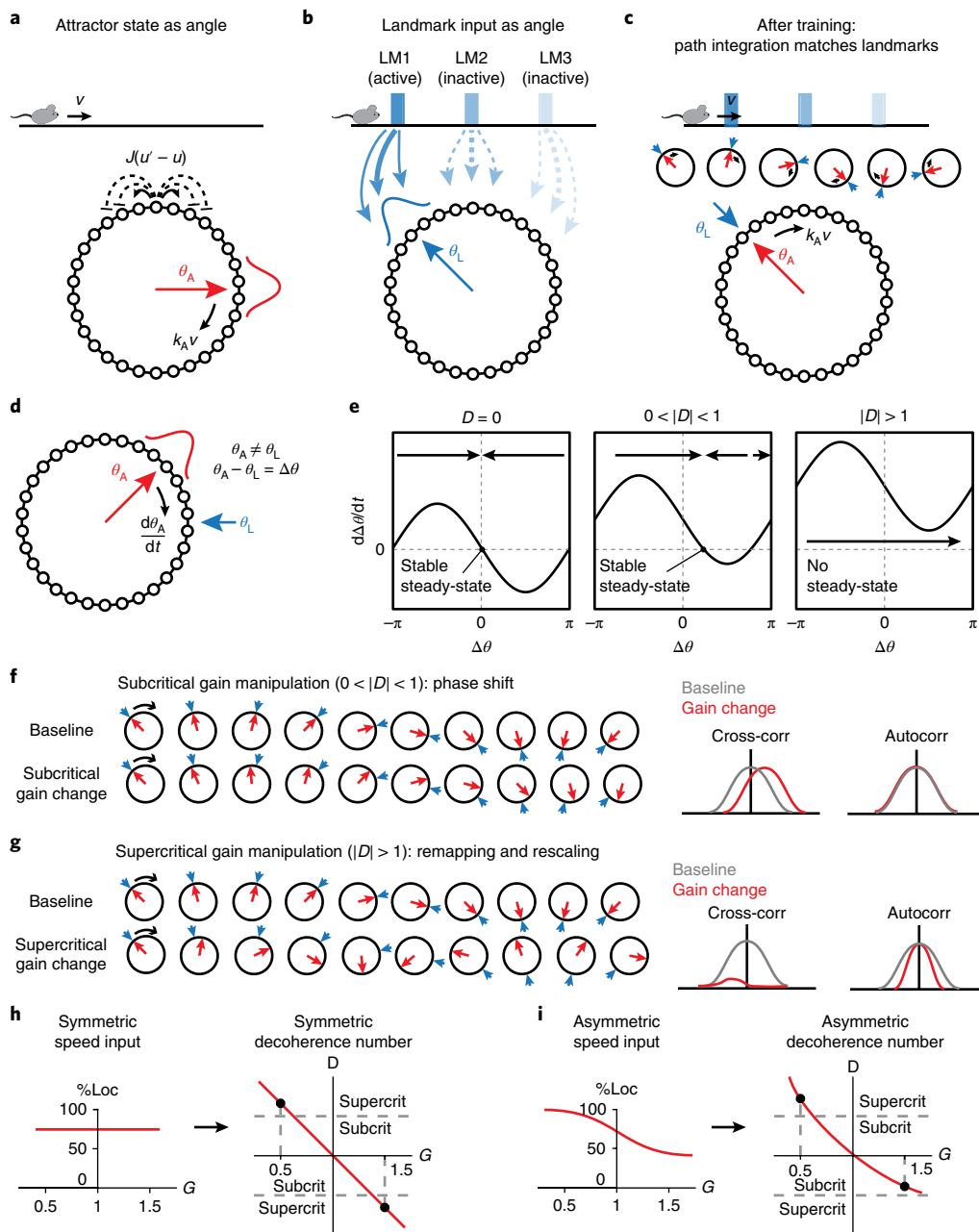
Fig. 5 | A coupled-oscillator attractor network model of the integration of landmarks and self-motion input by grid cells. a, Without landmarks, the model is a 1D ring attractor, with short-range excitation and long-range inhibition, as captured by translationally symmetric synaptic weights $J(u' - u)$ from position u to u' on the ring. This synaptic weight profile creates a set of steady-state 'bump' patterns that can be described by the phase angle θ_A of peak activity. When conjunctive velocity tuning is added and the synaptic weight profiles are offset in the direction of preferred velocity, velocity inputs move the bump around the attractor at a rate given by $k_A v$. **b**, Landmark input to the attractor network pins the attractor phase to a certain phase θ_L that depends on the position of the landmarks. **c**, Hebbian learning alters the learned landmark pinning phase θ_L (blue arrows) to make it consistent with attractor phase θ_A (red arrows), which advances as a result of path integration (black arrow). **d**, Illustration of a gain change, in which landmark input and path integration disagree ($\theta_A \neq \theta_L$). Landmark input draws the attractor phase θ_A to the pinning phase θ_L with a force that grows with the level of disagreement $\Delta\theta = \theta_A - \theta_L$ as $-\sin(\Delta\theta)$. **e**, Solutions to the model equations. $D = 0$ is the baseline condition (no gain change). When $|D| < 1$, $\Delta\theta$ settles into a steady state in which the attractor phase either leads or lags the landmark phase at a constant phase shift (subcritical regime). When $|D| > 1$, no steady state exists, and the difference between the attractor phase and the landmark phase will continually change (supercritical regime). **f**, The attractor phase (red arrows) and landmark phase (blue arrows) during baseline (top row) and gain change (bottom row) in the subcritical regime ($0 < |D| < 1$). Right: cartoons of the expected A–B cross- and autocorrelations (cross-corr and autocorr) in the subcritical regime. Note the similarity to the gain increase response (Fig. 3b). **g**, Same as **f**, but in the supercritical regime ($|D| > 1$), where the grid pattern breaks free of landmark inputs and rescales. Note, however, that even in this regime the influence of landmarks is still present, leading to a small peak in the cross-correlation and an incomplete rescaling of the pattern (Supplementary Math Note). We observed these effects in grid cells during gain decreases (Fig. 3b). **h,i**, If ω is constant, then a speed input that linearly integrates locomotion and visual speed can only lead to both supercritical (supercrit) or both subcritical (subcrit) responses to symmetric gain manipulations (**h**). By contrast, gain-dependent integration of visual and locomotor cues, as we observed in our speed cell data (Fig. 4), can explain the asymmetric grid cell response to gain manipulations (**i**).

observed during gain decreases contributed to a reduction in the strength of landmark input (Fig. 3b), the firing rates of border and other spatially stable cells did not change during gain manipulations (Supplementary Figs. 6, 8, 12 and 13). This suggests that the asymmetry in grid cell gain change responses does not reflect differences in landmark input strength (ω). Finally, gain-dependent integration of visual and locomotor speed cues in the velocity input to the attractor, as was observed in speed cells, could lead to asymmetrical grid responses (Fig. 5h,i). Using our experimentally measured speed cell data, we calculate that $|D_{g.d.}|$ in the gain decrease (g.d.) condition exceeds $|D_{g.i.}|$ in the gain increase (g.i.) condition by a factor of 1.9 (95% CI 1.2–3.0) (Supplementary Math Note). This difference in $|D|$ thus drives the grid cell responses into the supercritical regime during gain decreases, while grid cell responses remain in the subcritical regime during gain increases, explaining the asymmetric grid response to the two gain manipulations.

The asymmetry of the grid cell response to gain increases and decreases can now be understood as follows. During gain increase, speed cells are driven more by optic flow than locomotion (Fig. 4). This makes the phase advance of the attractor more similar to the rate of advance of visual landmarks. Thus, there is only a weak disagreement between path integration and landmarks, leading to the subcritical regime ($|D| < 1$) in which grid cells shift relative to baseline. In contrast, during gain decrease, speed cells are more strongly driven by locomotion. Thus, there is a larger disagreement between path integration and landmarks, leading to the supercritical regime ($|D| > 1$) in which the attractor phase breaks free from landmark correction and grid patterns rescale and remap. Generalization of this framework to 2D gave similar results (Supplementary Math Note).

However, despite the match between experimental observations and model predictions based on grid and speed cell population responses, the responses of individual pairs of speed and grid cells were uncorrelated (Supplementary Fig. 14). This suggests that grid cells either integrate input from many MEC speed cells, such that the correlation with any individual speed cell is weak, integrate input from a specific subset of speed cells that our methods could not identify, or receive speed information from another source.

Grid cell responses to an intermediate gain change follow the predictions of the model. To further test our model, we recorded grid cells in a third gain change condition, gain = 0.75 ($n = 11$ grid cells from 5 mice; Fig. 6). We used our model to predict how grid cells should respond to this gain change. First, we defined the percent mismatch between landmarks and self-motion as %Loc × |gain−1|, where %Loc is the percent locomotion in the speed input to the attractor (Supplementary Math Note). This mismatch, when large enough, drives grid cells into the supercritical regime. Since visual and locomotor cues were weighted roughly equally by speed cells at gain = 1.5 (Fig. 4), we estimated that our gain increase experiments created a 25% mismatch between landmarks and self-motion, rather than the 50% mismatch that would have been created if speed inputs were purely locomotor at this gain value. While we are unsure of the weighting of locomotor and visual speed inputs at gain = 0.75 (Fig. 6a), the maximum amount of mismatch that could be generated by gain = 0.75 is 25%, which would occur if speed inputs were 100% locomotor. Thus, the maximum possible decoherence number for gain = 0.75 is equal and opposite to the decoherence number for gain = 1.5 (Fig. 6a). Therefore, since responses to gain = 1.5 were within the coherent regime, the model strongly predicts that gain = 0.75 will be within the coherent regime and that grid fields will shift backwards on the track by an amount less than or equal to the amount that they shifted forward during gain = 1.5, without rescaling. Strikingly, this is what we observed in our data (Fig. 6b–e), providing further support for our model (Supplementary Fig. 15).

Integration of visual and locomotor cues in a path integration task. Finally, we asked whether the cue combination principles observed in grid and speed cells are reflected in behavior. We developed a path integration task wherein mice were trained to run 200 cm along a virtual track for an automatic water reward (Fig. 7a). Trials were interleaved with periods of complete darkness that varied in length (30–130 cm long). No fixed landmarks were present on the track but black and white squares that were randomized on each trial provided optic flow. Recordings from a similar VR track showed that grid cells remained stable for up to 200 cm and speed cell signals remained intact, suggesting that these signals were available in this task (Supplementary Fig. 16).

Leveraging the tendency of mice to spontaneously slow in anticipation of reward (Fig. 7b and Supplementary Video 1), we omitted rewards on a subset of trials (1 in 5) and used the running speed trajectory of the mouse as a readout of its perceived location (Fig. 7c). In reward omission trials, distance from the onset of the visual cues was more predictive of running speed than time (all $P < 1 \times 10^{-6}$, $n = 3$ mice; Supplementary Fig. 17). Therefore, in this task, mice integrated some combination of visual and locomotor speed to compute distance traveled. We then interleaved a subset of gain change trials (1 in 5, counterbalanced with reward omission trials; Fig. 7a). Gains were chosen such that the average real distance run on the track remained constant, to avoid retraining the mouse to run a different distance (gain decreases 0.92, 0.86, 0.8, 0.75; gain increases 1.09, 1.2, 1.33, 1.5). We used average running speed traces in gain change reward omission trials to compute the relative contributions of visual and motor speed cues to animals' distance estimates (Methods). Like grid cells and speed signals, mice weighted visual cues more during gain increases than gain decreases (Fig. 7d,e). This demonstrates that the asymmetrical gain change responses observed in the electrophysiological data extend to behavior.

Discussion

Here we found principled regimes under which behaviorally measured position estimates and MEC codes differentially weight the influence of visual landmark and self-motion cues. First, we found that conflicts between locomotion and visual cues caused grid cells to remap in an asymmetric manner, with gain increases causing phase shifts and gain decreases causing grid scale changes. This asymmetry was mirrored by multiple MEC speed signals. Second, we developed a coupled-oscillator attractor model that explained how grid responses to gain manipulations could arise from competition between conflicting self-motion and landmark cues. This model successfully predicted grid responses to an intermediate gain change. Finally, we used a path integration task to demonstrate a behavioral asymmetry in the weighting of visual versus locomotor cues that matched grid and speed responses. Taken together, these findings provide a framework for understanding the dynamics of cue combination in MEC neural codes and navigational behavior. This framework could be useful in interpreting grid cell responses to different environmental geometries, in which distortion[13,19], shearing[15], spatial frequency changes[14,32] or remapping[33,34] could reflect competition between landmark and self-motion inputs or context- or experience-dependent changes in these inputs[13,18]. We have begun to explore the implications of our model for these situations[29].

Our combined experimental and modeling results indicate that asymmetric speed input is likely to be the cause of the asymmetric grid response to gain manipulations, but the origin of and reasons for this asymmetry remain to be determined. Inputs from visual cortex, where both locomotion and optic flow influence the speed tuning of neurons[35], compose a substantial fraction of cortical inputs to MEC[36–38] and could include signals that are asymmetric with respect to VR gain. For example, visual cortex receives thalamic projections that respond to the degree to which running speed exceeds visual
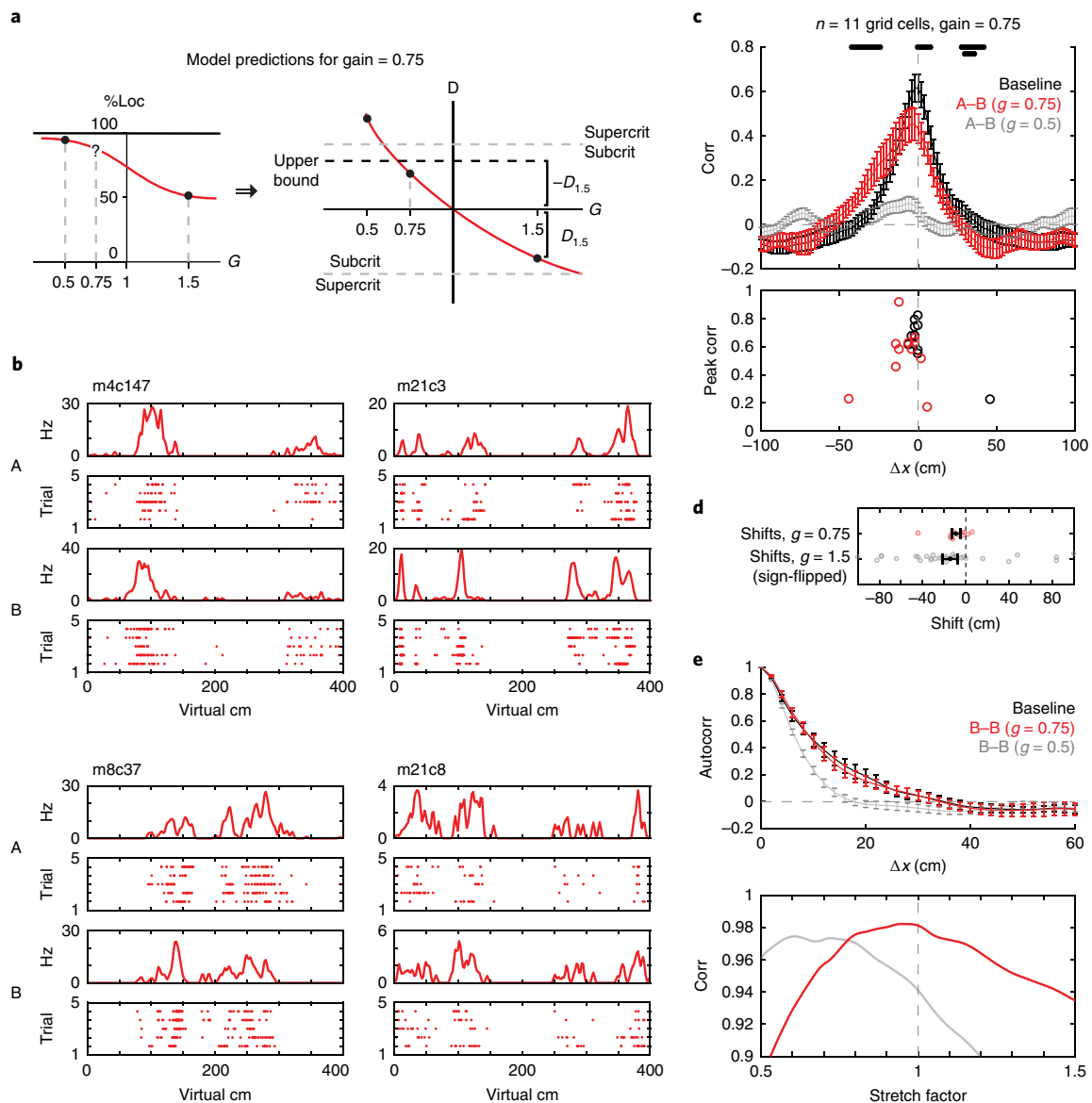
Fig. 6 | Grid cell responses to an intermediate gain value follow the predictions of the model. a, Model predictions for gain = 0.75. Using our speed cell data (left), the model predicts that the decoherence number during gain = 0.75 is bounded above by $-D_{1.5}$, where $D_{1.5}$ is the decoherence number for gain = 1.5 (right; see Results for argument). This predicts that gain = 0.75 should be within the subcritical (subcrit) regime and that grid cell firing patterns should shift backwards on the track, without rescaling, by an amount less than or equal to the forward shifts during gain = 1.5. **b**, Example grid cell responses to gain = 0.75. **c**, Top: average cross-correlations (corr) between rate maps generated from the A and B periods of gain = 0.75 manipulations (red), with adjacent blocks of 5 trials within baseline periods (black). Average A–B cross-correlations for gain = 0.5 manipulations are shown in gray for comparison ($n = 33$). Black dots indicate locations at which the red and black traces significantly differed (one dot, paired t-test $P < 0.05$; two dots, $P < 0.01$; no correction for multiple comparisons). Bottom: locations of the peaks of the A–B and baseline cross-correlations of individual cells (red, gain = 0.75; black, baseline). Cross-correlation peaks were shifted backward compared to baseline (shift ± s.e.m., gain = 0.75, –9.3 ± 4.0 cm; baseline, –2.5 ± 4.4 cm; one-sided Wilcoxon test $P = 0.027$). **d**, Grid cell shifts during gain = 0.75 and gain = 1.5. The signs of shifts at gain = 1.5 (which were forward along the track) have been flipped to directly compare them with shifts at gain = 0.75 (which were backward along the track). The model predicts that backward shifts during gain = 0.75 should be less than or equal to forward shifts during gain = 1.5. That is what we observed in the data (shift ± s.e.m., gain = 0.75, –9.3 ± 4.0 cm, $n = 11$; sign-flipped shift ± s.e.m., gain = 1.5, –14.4 ± 7.1 cm, $n = 37$; Wilcoxon rank sum $P = 0.14$). **e**, Average rate map autocorrelations during the B period of gain = 0.75 manipulations (red; $n = 11$), the B period of gain = 0.5 manipulations (gray; $n = 33$), and baseline (black; $n = 11$). As predicted by the model, we did not observe significant rescaling in gain = 0.75. Error bars: mean ± s.e.m.

speed[39]. In addition, MEC receives projections from extrastriate visual cortical regions that preferentially respond to fast-moving stimuli[37,40,41]. These inputs are presumably important for processing visual stimuli during running and could be more activated during gain increases. Intriguingly, it is precisely in the gain increase condition that optic flow is a more salient cue for speed, compared to

locomotion, suggesting that the increased reliance on visual cues for computing speed during gain increases may be consistent with optimal Bayesian principles for cue combination[42].

The ability of the path integration system to operate in both subcritical and supercritical regimes likely serves an adaptive purpose during navigation. For example, the subcritical regime is appropriate
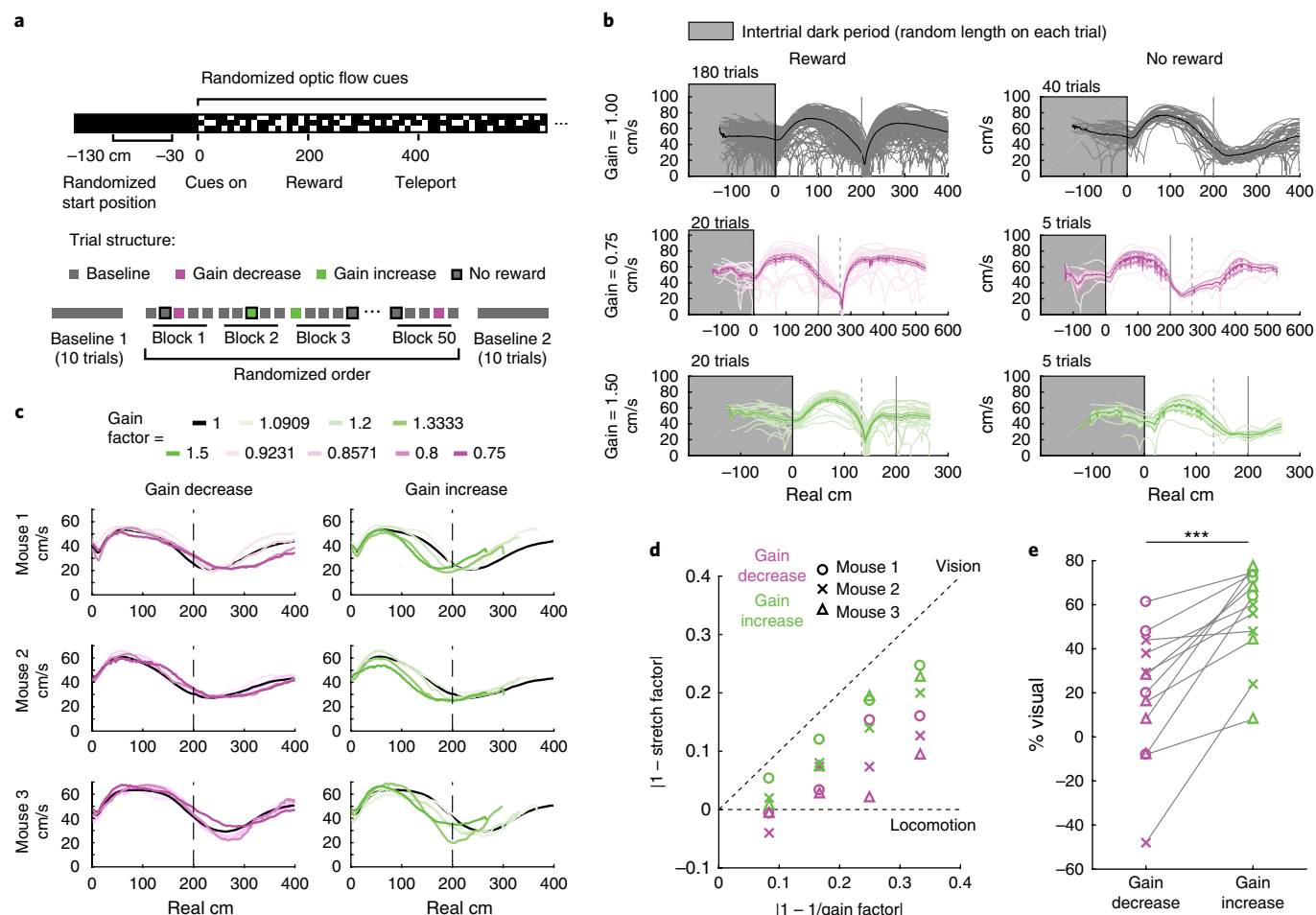
Fig. 7 | Integration of visual and locomotor cues in a path integration task. a, Schematic of the task. Animals were trained to run 200 cm along an infinite-perspective landmark-free VR track for water reward. At 400 cm the animal was teleported to a random starting position between –130 and –30 cm and the screens were set to black. When the animal reached 0 cm, visual cues came on. Visual cues consisted of black and white squares on the floor, ceiling and walls that were randomized each trial. After training, normal trials were interleaved with trials in which the reward was omitted (1 of 5) or the gain was changed (1 of 5, counterbalanced with reward omission). **b**, Behavior from an example session. Thin lines show running speed traces from individual trials; thick lines with shading show mean traces ± s.e.m. Mice spontaneously slowed down before the reward. In reward omission trials, the speed profile of the mouse could be used to estimate its perceived location on the track. **c**, Average running speed profiles in gain change, reward omission trials for 3 mice (location of minimum running speed in reward omission trials, mean ± s.d.: mouse 1, 243 ± 26 cm, $n = 41$ sessions; mouse 2, 237 ± 13 cm, $n = 41$ sessions; mouse 3, 268 ± 21 cm, $n = 49$ sessions). The overshoot beyond 200 cm likely reflects the mouse's inertia on the running wheel. **d**, Optimal stretch values for correlating baseline speed profiles with gain changed speed profiles. The 1:1 line represents fully visual behavior and the $y = 0$ line represents fully locomotor behavior. **e**, Optimal stretch factors from **d** were converted to percent weighting of visual cues. Mice used visual cues significantly more in gain increase trials than gain decrease trials (% visual ± s.e.m.: gain decrease, 19 ± 9%; gain increase, 56 ± 6%; $n = 12$ (4 conditions × 3 mice), Wilcoxon $P = 4.8 \times 10^{-4}$). Note the similarity with the percentages estimated from speed cells (gain decrease, 12 ± 12% visual; gain increase, 53 ± 14% visual; Fig. 4i). *** $P < 0.001$.

when landmark input is close enough to path integration to be used for error correction[12]. However, if landmarks change location or become unreliable, creating a large disagreement between landmark input and path integration, the network can enter the supercritical regime and pull free from the influence of landmarks. The decoherence threshold could therefore reflect the animal's expectations about the reliability of landmark input[42]. This idea that nonlinear cue integration serves an adaptive purpose during navigation may be a more general principle of parahippocampal computation. Recent work used VR gain changes to show that hippocampal place cells integrate visual and locomotor information nonlinearly[21]. These data strongly resemble the subcritical regime of our model, raising the possibility that some of the principles we reveal governing the integration of different information sources by both MEC neural codes and behavior may generalize to other brain regions that support navigation[43–46].

Methods

Methods, including statements of data availability and any associated accession codes and references, are available at https://doi.org/10.1038/s41593-018-0189-y.

References

1. Rowland, D. C., Roudi, Y., Moser, M. B. & Moser, E. I. Ten years of grid cells. *Annu. Rev. Neurosci.* **39**, 19–40 (2016).
2. Hafting, T., Fyhn, M., Molden, S., Moser, M. B. & Moser, E. I. Microstructure of a spatial map in the entorhinal cortex. *Nature* **436**, 801–806 (2005).
3. Taube, J. S., Muller, R. U. & Ranck, J. B. J. Jr. Head-direction cells recorded from the postsubiculum in freely moving rats. I. Description and quantitative analysis. *J. Neurosci.* **10**, 420–435 (1990).

4. Sargolini, F. et al. Conjunctive representation of position, direction, and velocity in entorhinal cortex. *Science* **312**, 758–762 (2006).

5. Aronov, D. & Tank, D. W. Engagement of neural circuits underlying 2D spatial navigation in a rodent virtual reality system. *Neuron* **84**, 442–456 (2014).

6. Solstad, T., Boccara, C. N., Kropff, E., Moser, M. B. & Moser, E. I. Representation of geometric borders in the entorhinal cortex. *Science* **322**, 1865–1868 (2008).

7. Hinman, J. R., Brandon, M. P., Climer, J. R., Chapman, G. W. & Hasselmo, M. E. Multiple running speed signals in medial entorhinal cortex. *Neuron* **91**, 666–679 (2016).

8. Kropff, E., Carmichael, J. E., Moser, M. B. & Moser, E. I. Speed cells in the medial entorhinal cortex. *Nature* **523**, 419–424 (2015).

9. McNaughton, B. L., Battaglia, F. P., Jensen, O., Moser, E. I. & Moser, M. B. Path integration and the neural basis of the 'cognitive map'. *Nat. Rev. Neurosci.* **7**, 663–678 (2006).

10. Winter, S. S., Mehlman, M. L., Clark, B. J. & Taube, J. S. Passive transport disrupts grid signals in the parahippocampal cortex. *Curr. Biol.* **25**, 2493–2502 (2015).

11. Winter, S. S., Clark, B. J. & Taube, J. S. Disruption of the head direction cell network impairs the parahippocampal grid cell signal. *Science* **347**, 870–874 (2015).

12. Hardcastle, K., Ganguli, S. & Giocomo, L. M. Environmental boundaries as an error correction mechanism for grid cells. *Neuron* **86**, 827–839 (2015).

13. Krupic, J., Bauza, M., Burton, S., Barry, C. & O'Keefe, J. Grid cell symmetry is shaped by environmental geometry. *Nature* **518**, 232–235 (2015).

14. Barry, C., Hayman, R., Burgess, N. & Jeffery, K. J. Experience-dependent rescaling of entorhinal grids. *Nat. Neurosci.* **10**, 682–684 (2007).

15. Stensola, T., Stensola, H., Moser, M. B. & Moser, E. I. Shearing-induced asymmetry in entorhinal grid cells. *Nature* **518**, 207–212 (2015).

16. Perez-Escobar, J. A., Kornienko, O., Latuske, P., Kohler, L. & Allen, K. Visual landmarks sharpen grid cell metric and confer context specificity to neurons of the medial entorhinal cortex. *Elife* **23**, e16937 (2016).

17. Chen, G., Manson, D., Cacucci, F. & Wills, T. J. Absence of visual input results in the disruption of grid cell firing in the mouse. *Curr. Biol.* **26**, 2335–2342 (2016).

18. Krupic, J., Bauza, M., Burton, S., Lever, C. & O'Keefe, J. How environment geometry affects grid cell symmetry and what we can learn from it. *Phil. Trans. R. Soc. Lond. B* **369**, 20130188 (2013).

19. Krupic, J., Bauza, M., Burton, S. & O'Keefe, J. Local transformations of the hippocampal cognitive map. *Science* **359**, 1143–1146 (2018).

20. Dombeck, D. A., Khabbaz, A. N., Collman, F., Adelman, T. L. & Tank, D. W. Imaging large-scale neural activity with cellular resolution in awake, mobile mice. *Neuron* **56**, 43–57 (2007).

21. Chen, G., King, J. A., Burgess, N. & O'Keefe, J. How vision and movement combine in the hippocampal place code. *Proc. Natl Acad. Sci. USA* **110**, 378–383 (2013).

22. Eggink, H., Mertens, P., Storm, I. & Giocomo, L. M. Hyperpolarization-activated cyclic nucleotide-gated 1 independent grid cell-phase precession in mice. *Hippocampus* **24**, 249–256 (2014).

23. Hardcastle, K., Maheswaranathan, N., Ganguli, S. & Giocomo, L. M. A multiplexed, heterogeneous, and adaptive code for navigation in medial entorhinal cortex. *Neuron* **94**, 375–387.e7 (2017).

24. Jeewajee, A., Barry, C., O'Keefe, J. & Burgess, N. Grid cells and theta as oscillatory interference: electrophysiological data from freely moving rats. *Hippocampus* **18**, 1175–1185 (2008).

25. McFarland, W. L., Teitelbaum, H. & Hedges, E. K. Relationship between hippocampal theta activity and running speed in the rat. *J. Comp. Physiol. Psychol.* **88**, 324–328 (1975).

26. Skaggs, W. E., Knierim, J. J., Kudrimoti, H. S. & McNaughton, B. L. A model of the neural basis of the rat's sense of direction. *Adv. Neural Inf. Process. Syst.* **7**, 173–180 (1995).

27. Burak, Y. & Fiete, I. R. Accurate path integration in continuous attractor network models of grid cells. *PLOS Comput. Biol.* **5**, e1000291 (2009).

28. Samsonovich, A. & McNaughton, B. L. Path integration and cognitive mapping in a continuous attractor neural network model. *J. Neurosci.* **17**, 5900–5920 (1997).

29. Ocko, S.A., Hardcastle, K., Giocomo, L.M. & Ganguli, S. Emergent elasticity in the neural code for space. Preprint at bioRxiv https://doi.org/10.1101/326793 (2018).

30. Fuhs, M. C. & Touretzky, D. S. A spin glass model of path integration in rat medial entorhinal cortex. *J. Neurosci.* **26**, 4266–4276 (2006).

31. Strogatz, S. H. From Kuramoto to Crawford: exploring the onset of synchronization in populations of coupled oscillators. *Physica D.* **143**, 1–20 (2000).

32. Stensola, H. et al. The entorhinal grid map is discretized. *Nature* **492**, 72–78 (2012).

33. Derdikman, D. et al. Fragmentation of grid cell maps in a multicompartment environment. *Nat. Neurosci.* **12**, 1325–1332 (2009).

34. Carpenter, F., Manson, D., Jeffery, K., Burgess, N. & Barry, C. Grid cells form a global representation of connected environments. *Curr. Biol.* **25**, 1176–1182 (2015).

35. Saleem, A. B., Ayaz, A., Jeffery, K. J., Harris, K. D. & Carandini, M. Integration of visual motion and locomotion in mouse visual cortex. *Nat. Neurosci.* **16**, 1864–1869 (2013).

36. Burwell, R. D. & Amaral, D. G. Cortical afferents of the perirhinal, postrhinal, and entorhinal cortices of the rat. *J. Comp. Neurol.* **398**, 179–205 (1998).

37. Wang, Q., Gao, E. & Burkhalter, A. Gateways of ventral and dorsal streams in mouse visual cortex. *J. Neurosci.* **31**, 1905–1918 (2011).

38. Koganezawa, N., Gisetstad, R., Husby, E., Doan, T. P. & Witter, M. P. Excitatory postrhinal projections to principal cells in the medial entorhinal cortex. *J. Neurosci.* **35**, 15860–15874 (2015).

39. Roth, M. M. et al. Thalamic nuclei convey diverse contextual information to layer 1 of visual cortex. *Nat. Neurosci.* **19**, 299–307 (2016).

40. Andermann, M. L., Kerlin, A. M., Roumis, D. K., Glickfeld, L. L. & Reid, R. C. Functional specialization of mouse higher visual cortical areas. *Neuron* **72**, 1025–1039 (2011).

41. Marshel, J. H., Garrett, M. E., Nauhaus, I. & Callaway, E. M. Functional specialization of seven mouse visual cortical areas. *Neuron* **72**, 1040–1054 (2011).

42. Knill, D. C. & Pouget, A. The Bayesian brain: the role of uncertainty in neural coding and computation. *Trends Neurosci.* **27**, 712–719 (2004).

43. Alexander, A. S. & Nitz, D. A. Retrosplenial cortex maps the conjunction of internal and external spaces. *Nat. Neurosci.* **18**, 1143–1151 (2015).

44. Elduayen, C. & Save, E. The retrosplenial cortex is necessary for path integration in the dark. *Behav. Brain Res.* **272**, 303–307 (2014).

45. Harvey, C. D., Coen, P. & Tank, D. W. Choice-specific sequences in parietal cortex during a virtual-navigation decision task. *Nature* **484**, 62–68 (2012).

46. Whitlock, J. R., Pfuhl, G., Dagslott, N., Moser, M. B. & Moser, E. I. Functional split between parietal and entorhinal cortices in the rat. *Neuron* **73**, 789–802 (2012).

Author contributions

L.M.G. and M.G.C. conceived experiments and analyses. C.S.M. and M.G.C. performed chronic implantations and M.G.C. collected and analyzed in vivo data. M.G.C. and I.I.C.L. collected behavioral data. S.A.O. and S.G. conceived modeling and simulations and S.A.O. performed them. L.M.G. and M.G.C. wrote the paper with feedback from all authors.

Competing interests

The authors declare no competing interests.

Additional information

Supplementary information is available for this paper at https://doi.org/10.1038/s41593-018-0189-y.

Reprints and permissions information is available at www.nature.com/reprints.

Correspondence and requests for materials should be addressed to M.G.C. or L.M.G.

Publisher's note: Springer Nature remains neutral with regard to jurisdictional claims in published maps and institutional affiliations.

Methods

Statistics. All data were analyzed in MATLAB. Unless otherwise noted, all tests are two-sided, correlation coefficients represent Pearson's correlation, values are presented as mean $\pm$ s.e.m., and n values indicate number of neurons. Only non-parametric tests were used to assess significance of results, specifically Wilcoxon signed-rank tests for paired data and Wilcoxon rank-sum tests for unpaired data. Data collection and analysis were not performed blind to the conditions of the experiments. All animals except mouse 1 experienced both gain decreases and gain increases, which were presented in a randomized order on each day. No statistical methods were used to predetermine sample sizes, but our sample sizes are similar to those reported in previous publications[21,22,47]. For additional information regarding sample sizes, statistics and reproducibility, please see the accompanying Life Sciences Reporting Summary.

Subjects. All techniques were approved by the Institutional Animal Care and Use Committee at Stanford University School of Medicine. Recordings were made from 21 C57BL/6 mice aged 6 weeks to 6 months at the time of surgery (18–28 g). All mice were female except mice 19 and 21, which were male. Mice were singly housed in transparent cages on a 12-h light-dark cycle and experiments were performed during the light phase.

In vivo surgery. Anesthesia was induced with isoflurane (4%; maintained at 0.5–3%) followed by injection of buprenorphrine (0.1 mg/kg). Mice were unilaterally implanted in the right hemisphere with a microdrive (Axona) carrying two (17 mice), four (3 mice) or eight (1 mouse) 17-µm platinum-iridium (90% and 10%, respectively) wire tetrodes and a custom-built metal headbar containing two holes for head fixation. Immediately before surgery, tetrodes were platinum electroplated to reduce the impedance to 200 k at 1 kHz. The microdrive was affixed to the skull using dental cement and jewelers' screws, one of which was used to ground the electrodes. The tetrodes were implanted 3.3–3.4 mm from the midline, 0.4–0.5 mm in front of the transverse sinus, and 800 µm below the dura at an angle of 0–2 degrees in the posterior direction in the sagittal plane.

Training. Following surgery, mice were singly housed and allowed free access to food and water for >3 d, after which they were water deprived. Each day, mice were given 1 mL of water and weighed to ensure that their weight remained above 80% of baseline. After 2 d of water deprivation, mice were accustomed to head fixation for 2 d (20 min/d) and trained to drink water from a custom lick port. They were then trained to run in virtual reality (see below) on a semi-infinite training track with small water rewards (~2 µL) delivered every 50 cm, until they ran an average of at least 5 cm/s in a 20-min training session. The training track was visually distinct from the track on which cells were recorded.

Data collection and spike sorting. The open field environment was a 90 × 90 × 30 cm black box with a white cue card attached to the middle of one wall. In some open field sessions, a smaller box was used (70 × 70 × 30 cm). The room was dimly lit, and some distal cues were visible. Mice were connected to the equipment via an AC-coupled unity-gain operational amplifier attached to a counterbalanced cable that allowed free movement through the arena. To track the mouse's position in the open field, the recording system tracked the position of two light-emitting diodes (LEDs), one large and one small, on the headstage by means of an overhead video camera. Position estimates in the open field were based on the tracking of these LEDs. Mice foraged for crumbled cereal until they had explored the entire box (coverage > 70%; 20 to 120 min). Between open field sessions, the test box was cleaned with soapy water.

After an open field recording session, mice were immediately transferred to the VR setup to minimize tetrode drift (Supplementary Fig. 3). In the VR setup, head-fixed mice ran on a 20-cm-diameter polystyrene ball (Graham Sweet Studios) or, in some cases, a 15.2-cm-diameter foam roller (ethylene vinyl acetate). Both were constrained to rotate about one axis. The ball's or cylinder's rotation was measured by a high-resolution quadrature encoder (Yumo, 1024 P/R) and processed by a microcontroller (Arduino UNO). The virtual environment was generated using commercial software (Unity 3D) and updated according to the motion signal. Virtual reality position traces were synchronized to recording traces using 1-Hz timing pulses generated by the recording software. The virtual scene was spherically corrected using video manipulation software (MadMapper) and back-projected onto a 35.6-cm transparent plastic hemisphere over which projector fabric was stretched. The projection covered 180° of the mouse's field of view horizontally and 90° vertically, with a black drape hanging from the plastic hemisphere edges to eliminate visual cues outside this field of view. In some experiments, the virtual scene was displayed on three 24-inch monitors surrounding the mouse. The gain of the linear transformation from ball rotation to translation along the virtual track was calibrated so that the virtual track was 4 m long. The standard cue-rich track contained three sections with distinct wall patterns and several distal landmarks (Fig. 1). During optic flow experiments, mice ran on a track with optic flow cues along the length of the track (Supplementary Fig. 16). At the end of the track, the mouse received a water reward (5 µL) and was teleported to the beginning of the track for the next

trial. Water rewards were delivered using a solenoid (Cole-Parmer) triggered from the virtual environment software, generating an audible click with water delivery.

Voltage signals were amplified and band-pass filtered between 0.8 and 6.7 kHz. Triggered spikes were stored to a disk at 48 kHz (50 samples per waveform). EEG was recorded from one of the electrodes and low-pass filtered at 500 Hz, sampled at 4,800 Hz and stored with the unit data. Spikes were sorted offline using Klustakwik[48] followed by manual curation of clusters. Only clusters with at least 100 spikes in open field and firing rate >0.2 Hz in VR were included. For inclusion in the manipulation sessions, the firing rate of a given neuron had to be at least 0.2 Hz in both the A and B periods. Cluster quality was assessed using spike waveform and the refractory period in the spike time autocorrelation. Clusters were matched manually between open field and VR, and the normalized center-of-mass distance between clusters was calculated to assess the quality of cluster matching (Supplementary Fig. 3). After all data collection in the open field and VR, tetrodes were moved ventrally by ≥25 µm.

Histology. At the end of recording, electrodes were not moved and a small electrolytic lesion was made at the last site at which cells were recorded (two 8-s pulses of 20 µA current). The mice were then killed with an overdose of pentobarbital and transcardially perfused with phosphate-buffered saline (PBS) followed by 4% paraformaldehyde. Brains were extracted and stored in 4% paraformaldehyde for at least 24 h. Brains were then rapidly frozen, cut into 30-µm sagittal sections with a cryostat, mounted and stained with cresyl violet. The positions of the tips of the recording electrodes were determined from digital pictures of the brain sections and the tetrode location was marked as the center of the lesion. Histological sections were examined to confirm that the recorded cells were located in the MEC, based on the reference Allen Brain Atlas and *The Mouse in Stereotaxic Coordinates*[49] (Supplementary Fig. 1).

Virtual reality behavior. Running speed in VR was computed by dividing the difference in position between adjacent time bins by the difference in time. This vector was then smoothed with a Gaussian kernel with s.d. = 10 bins (~170 ms). Average running speeds at each location on the track were computed by averaging the instantaneous speeds that occurred within each position bin (bin size = 2 cm; Supplementary Fig. 2c,e). To compute the angular velocities experienced by the mouse during running, we converted running speed into angular velocity as a function of location on the hemispherical screen by empirically measuring the displacement of the visual cues in degrees following fixed rotations of the ball (Supplementary Fig. 2d). At running speeds of 35 cm/s, which were typical along the length of the track (Supplementary Fig. 2c), angular velocities ranged from 0° s^{-1} in front of the mouse (at infinity) to 240° s^{-1} at the edge of the screen, well within the range of speeds that optimally drive V1 neurons in mouse[40]. To check whether VR behavior varied over sessions, we computed average running speed in each of the first 30 trials for sessions in which there were no gain manipulations (Supplementary Fig. 2b).

For gain manipulations, the animal performed ≥15 trials with gain = 1 (A), 5 or 10 trials with altered gain (B), and ≥15 trials with gain = 1 (A′) (Fig. 2). In gain increase sessions, animals ran 10 B trials to allow the collection of a greater number of spikes. In some gain manipulation experiments, the mouse ran several alternating blocks of baseline and gain change. Each baseline block had at least 15 trials, and each gain change block was either 5 trials (gain decrease) or 10 trials (gain increase).

Linear path integration behavioral task. Three female C57BL/6 mice age 3–6 months were trained on the VR linear path integration task (Fig. 7). Two of these mice had tetrode implants; electrophysiological data from one was included in this study (m18). The third mouse was implanted with a headbar, but no tetrode drive. Mice were accustomed to head fixation, water-deprived, and trained to lick water from the lick port following the same procedure as the tetrode-implanted mice. Following this initial training, mice were exposed to the VR path integration track but with the reward at 100 cm rather than 200 cm, with rewards omitted 1 in every 5 trials but no gain changes. When they started to slow at the reward location (mean speed within 25 cm of the reward site had to be ≥10 cm/s less than the mean speed between 0 and 50 cm from the start of the track), the reward location was moved to 150 cm. When they passed this same criterion with the reward at 150 cm, the reward was moved to 200 cm, and when they passed at 200 cm, they were considered fully trained. To compute average speed traces (Fig. 7b,c), mean speed in each position bin (bin size = 2 cm) was computed for each trial and then averaged across trials. Out of 10 mice that began training, 3 reached completion by meeting the criteria described above. The other 7 mice failed to progress beyond one of the steps described above. After completing training, mice ran sessions in which, following an initial block of 10 baseline trials, the gain was changed in 1 out of every 5 trials. These trials were counterbalanced with reward omission trials, such that on 1 in 5 gain change trials the reward was also omitted. On a given gain change session, two gains were used: one gain decrease (one of 0.92, 0.86, 0.8 or 0.75) and one gain increase (one of 1.09, 1.2, 1.33 or 1.5), matched such that the average distance on the track remained constant.

To compute mutual information between running speed and either distance or time (Supplementary Fig. 17a), we used the formula:

$$\text{M.I.} = \sum_i \sum_j p(x_i, s_j) \log \left[\frac{p(x_i, s_j)}{p(x_i)p(s_j)} \right]$$

where x is either distance or time since the start of the trial, s is the running speed of the mouse, $p(x_i, s_j)$ is the probability that distance or time is in bin i and speed is in bin j, $p(x_i)$ is the probability that distance or time is in bin i, and $p(s_j)$ is the probability that speed is in bin j. Here the ranges of each variable (distance or time and running speed) were split into 200 bins each. Mutual information was calculated for each session separately. Gain change trials were excluded from this analysis.

To compute the percent weighting of visual cues during gain changes, baseline average speed traces were stretched by varying amounts and correlated with gain changed running speed profiles. The stretch factor with the highest correlation was chosen. We then plotted $\left| 1 - \frac{1}{\text{gain factor}} \right|$ versus $|1 - \text{stretch factor}|$ (Fig. 7d). Taking the absolute value displayed gain decreases and gain increases on the same axis, and taking the reciprocal of the gain factor was necessary because this analysis was done in real, not virtual, coordinates. Fully visual behavioral responses will lie along the 1:1 diagonal whereas fully locomotor behavioral responses will lie on the $y = 0$ line. We converted each of these points to a percentage (Fig. 7e) by computing

$$\text{percent}_{\text{visual}} = 100 \times \frac{|1 - \text{stretch factor}|}{\left| 1 - \frac{1}{\text{gain factor}} \right|}$$

To test whether responses to gain manipulations systematically changed over time, possibly reflecting a slow learning or sensitization process, we computed visual percentages in each session separately and plotted them as a function of session number (Supplementary Fig. 17b).

Cell type classification. Cell type classification was based on open field recordings. To characterize open field firing fields, position data were binned into 2.5×2.5 cm bins and the path was smoothed with a 21-sample boxcar window filter. Maps for number of spikes and time were smoothed separately using a quasi-Gaussian kernel over the adjacent 5×5 bins[50]. All data were speed filtered and only epochs of instantaneous running speeds ≥ 2.5 cm/s included. Putative excitatory cells were separated from putative interneurons on the basis of mean open field firing rate. Putative interneurons ($n = 79$) had mean firing rate > 10 Hz in the open field. Putative excitatory cells ($n = 702$) were then classified as grid and border using published scores[4,6,50]. An adaptive smoothing method was used before the calculation of grid and border scores. To identify grid cells, we generated a grid score by taking a circular sample of the autocorrelation centered on the central peak and comparing it to rotated versions of the same circular sample (60 and 120 versus 30°, 90° and 150°)[50]. Border cells were identified using a previously published border score[6]. To define head direction cells, we plotted the firing rate of a neuron relative to the mouse's directional heading, divided into 0.5-degree bins and smoothed with a 14.5-degree mean window filter. The strength of directional tuning was defined as the length of the mean vector for the circular distribution of firing rate. See "Speed cell analyses" for classification of speed cells.

To determine score thresholds for cell classification, we performed a shuffling procedure[50]. For each cell, spikes were time shifted along the animal's recorded trajectory by a random interval (ranging from 20 ms to the total trial length minus 20 ms), with the end of the trial wrapped to the beginning. This procedure was repeated 100 times for each cell, with a firing rate map and relevant score (grid score, border score, mean vector length score) computed for each permutation. Cells were classified as a particular functional cell type when their score exceeded the 95th percentile of scores generated in the shuffled dataset (grid score P95 = 0.349, border score P95 = 0.523, head direction score P95 = 0.154)[50,51]. Spatial VR cells (Supplementary Fig. 12) were defined as cells that were not classified as grid, border or head direction, but had spatial stability > 0.5 in VR (see "Grid and border cell analyses" for definition of spatial stability).

Grid and border cell analyses. *Spatial stability in VR.* In the VR environment, firing rate vectors were generated by splitting the track into 2-cm bins and dividing the number of spikes in each bin by the dwell time in that bin. Periods when the mouse's speed was less than 2 cm/s were excluded from analysis. The resulting firing rate vector was smoothed using a Gaussian filter (s.d. = 2 cm). Spatial stability was defined as the correlation of the firing rate map generated separately in the first versus second half of the recording session.

Firing patterns of grid and border cells during baseline sessions. To check for non-uniformities in grid and border cell firing rate across the track (Fig. 1e), we analyzed grid and border cells with spatial stability > 0.2, ensuring that the cells had significant positional tuning. Repeated-measures ANOVA with Greenhouse–Geisser correction was used to test for the influence of spatial position on the population firing rate of grid and border cells (Fig. 1e). To create the percentiles

shown on the average tuning curve plot (Fig. 1e), 2-cm spatial bins were shuffled randomly with respect to the track, differently for each cell (1,000 shuffles). Then the 5th, 50th and 95th percentiles of firing rate were computed for each spatial bin in the shuffled data.

Grid and border cell analyses in gain manipulations. To analyze changes in grid and border cell firing patterns during gain changes, we compared the A and the B period of gain manipulation sessions. While the A period was usually 15 or more trials, for these analyses we only used the last n trials of A, where n is the number of trials in B, thereby matching the number of trials between the two periods. To be kept for analysis, cells had to have a firing rate of at least 0.2 Hz and stability > 0.2 in both periods. The firing patterns of this set of cells, which were the majority, were therefore nonrandom and could be meaningfully analyzed. Some cells were recorded during multiple gain manipulations. For these cells, gain manipulation sessions that passed the firing rate and stability thresholds were analyzed separately and then averaged together before reporting final statistics. All analyses of grid and border cell responses to gain manipulations were performed in the virtual reference frame; that is, with respect to virtual position on the track rather than real distance run on the ball.

Computing cross-correlations and autocorrelations. Cross-correlations were computed between the A- and B-period firing rate maps, and autocorrelations were computed for the two periods separately for grid and border cells (Figs. 3b,c and 6c,e), as well as spatial VR cells (Supplementary Fig. 12d–f) and head direction cells (Supplementary Fig. 13d–f). To estimate the percent rescaling from autocorrelations, the mean baseline (A period) autocorrelation map was stretched by different amounts (0.5 to 1.5 in increments of 0.01) and correlated with the average gain change (B period) autocorrelation map, using linear interpolation where necessary to match the stretched A-period data to the B-period data (Figs. 3c and 6e and Supplementary Figs. 12f and 13f). This was also done for each grid cell individually (values reported in the Results). In addition, for grid and border cells, we computed firing rate on single trials, in the same manner as the full session, and created single-trial autocorrelation maps that were then averaged across trials (Supplementary Fig. 7d) or shown for each trial individually (Supplementary Fig. 7e). This allowed us to include unstable cells (stability < 0.2), which may have firing rate maps that drift across trials but consistent field size from trial to trial. To test whether scale changes were due to a simple rescaling of the baseline pattern, baseline firing rate maps were stretched (0.5 to 1.5 in increments of 0.01) and correlated with gain change maps. The average correlation at each stretch value was computed for grid and border cells in gain increases and gain decreases (Supplementary Fig. 6g).

Outer products of firing rate maps. We visualized A–B cross-correlations across all locations on the track by computing average outer products between the A- and B-period firing rate maps (Supplementary Fig. 8a). Specifically, for each cell we normalized the A- and B-period firing rate vectors by subtracting the mean and dividing by the s.d. Then we computed the outer product matrix, whose i,jth entry is

$$\widehat{frA_i} \cdot \widehat{frB_j}$$

where $\widehat{frA_i}$ is the normalized firing rate at position i in the A period and $\widehat{frB_j}$ is the normalized firing rate at position j in the B period. Outer product matrices were averaged across cells. Outer products were also taken between the A period and itself and the B period and itself.

Computing cross-correlations and autocorrelations for different track segments. We checked whether the phase shifts and scale changes seen in grid cells varied across the track by computing cross- and auto-correlations in the three segments of the track with different patterns on the walls, which could possibly be associated with different strengths of landmark input (Supplementary Fig. 8b,c). Population averages of cross- and autocorrelations in these three track segments were computed, and cells were also analyzed individually. Locations of peaks in the cross-correlation were used to identify the phase shift for each cell, and the scale changes were estimated by identifying the point at which the single-cell firing rate autocorrelation fell below 0.2. One-way ANOVA on individual cells' phase shifts and scale changes did not identify differences between these values in different segments of the track (Supplementary Fig. 8b,c).

Identification of significant grid and border firing fields. To further analyze individual cells' responses, we identified significant firing fields in grid and border cells as follows (Supplementary Fig. 6b)[52]. First, shuffled firing rate distributions were created by shuffling spikes by a constant temporal offset (ranging from 20 ms to the total trial length minus 20 ms), which was different for each trial, 1,000 times and recomputing the smoothed firing rate for each permutation. Then firing fields were identified as contiguous groups of at least three bins that exceeded the 85th percentile of the shuffled distribution. Fields were extended by no more than one bin to the left and/or right if this adjacent bin exceeded the 70th percentile of the shuffled distribution. Fields were excluded if they did not have spikes on more than

20% of trials, thus excluding fields that had spikes on only 1 of 5 trials during gain decreases or 2 of 10 trials during gain increases. Fields were combined if there was only one non-field bin separating them.

Analysis of grid cells on a real linear track. Spiking data from grid cells recorded while animals navigated a real linear track (Supplementary Fig. 4g) were taken from a published study[22]. This dataset contained 64 grid cells from 7 male mice. Grid cells were identified on the basis of separate open field recordings in exactly the same manner as in the rest of this paper. Linear track sessions were split into left-moving and right-moving epochs on the basis of speed thresholds of >2 cm/s (right-moving) and <-2 cm/s, after the speed trace had been smoothed with a Gaussian kernel (s.d. = 200 ms). Half-and-half stability was computed for left-moving and right-moving epochs separately and then averaged together by cell (Supplementary Fig. 4h).

Speed cell analyses. We identified speed cells as follows. Instantaneous speed was calculated by dividing change in position by change in time for each temporal bin (OF = 20 ms, VR = 16.7 ms). Periods when the animal moved <2 cm/s or >100 cm/s were removed. The speed trace was smoothed with a Gaussian kernel (s.d. = 10 bins, or 200 ms in OF, 167 ms in VR). Instantaneous firing rate was estimated by smoothing the vector of spike counts in each time bin with a Gaussian kernel (s.d. = 20 bins, or 400 ms in open field, 334 ms in VR). The speed score was defined as the Pearson correlation between instantaneous speed and instantaneous firing rate[8]. The speed slope and intercept were calculated using least-squares linear regression. We identified speed cells as neurons with speed score higher than the 95th percentile of shuffled distributions in both open field and VR (P95 open field = 0.06, P95 VR = 0.12; shuffling procedure performed in the same manner as that for grid, border and head direction cells). Because running speed and position were correlated in the VR environment (Supplementary Fig. 2), we next split the track into eight 50-cm bins and required that the average of the speed scores calculated separately in each bin, weighted by the number of spikes in each bin, be greater than the 95th percentile of a shuffled distribution (P95 = 0.10). Specifically, this score was

$$\rho_{binned} = \frac{\sum_{i=1}^{8} n_i \rho_i}{n}$$

where n is the total number of spikes, i is the spatial bin (one of eight 50-cm bins along the 400-cm track), n_i is the number of spikes in the ith bin, and ρ_i is the speed score calculated in the ith bin. For gain manipulation sessions, speed cells had to meet the two VR criteria in both the A and the B periods, as well as the open field criterion. Speed cell response to gain manipulations was analyzed by calculating the speed score relative to real running speed (real cm/s) because speeds did not vary between baseline and gain changes (Supplementary Fig. 2), making it more straightforward to compare data in these coordinates. To visualize speed cell data, we split the range of running speed and instantaneous firing rate into 10 bins each and created 2D heat maps in which the intensity of each bin was proportional to the amount of time that speed and firing rate were within that bin (for example, Fig. 4b).

To calculate the degree to which visual versus locomotor cues drove speed cells during gain changes, we examined the slopes of linear fits to A- and B-period data (Fig. 4). These slopes were converted to an angle as follows:

$$\theta = \arctan\left(\frac{slope_B}{slope_A}\right)$$

Because all slopes were positive by the definition of speed cells, these angles ranged between 0 and $\pi/2$ (0 and 90°). We converted angles into percent visual weights as follows:

$$percent_{visual} = 100 \times \frac{\arctan(G) - \theta}{\arctan(G) - \frac{\pi}{4}}$$

where G is the gain factor (0.5 in gain decrease, 1.5 in gain increase). As a control, we performed the same analyses on data from the A′ period (Supplementary Fig. 10a). Only the first 10 trials of the A′ period were used to match trial numbers with gain increases. Finally, quadratic fits to data were computed in addition to linear fits using least-squares regression (Supplementary Fig. 10b):

$$fr = \theta_0 + \theta_1 s + \theta_2 s^2$$

where fr is instantaneous speed cell firing rate and s is instantaneous running speed. We added the constraints $\theta_0 \geq 0$, $\theta_1 \geq 0$ and $\theta_2 \leq 0$ to give these fits a saturating shape.

Theta analyses. We analyzed local field potential (LFP) theta oscillations as follows. For each session, LFP signals were extracted and sampled at 250 Hz, and a theta score was calculated as the ratio between power in the 6–10 Hz band and the 10–14 Hz band. To proceed, we required that this score be greater than 3. We then pooled data by mouse by concatenating LFP traces from multiple sessions.

This step was necessary because individual sessions, with 5 or 10 gain change trials, were too short to adequately estimate theta frequency–running speed slopes. We excluded mice with fewer than 3 sessions with significant theta for the same reason (3 mice excluded: m4, m17 and m20). One mouse did not run any gain increase sessions (m1). This left 17 mice with 89 sessions (gain decrease) and 16 mice with 95 sessions (gain increase). We filtered the LFP using a third-order bandpass Butterworth filter between 4 and 12 Hz, computed the power spectrum and found the frequency with peak power in baseline, gain decrease and gain increase (Supplementary Fig. 11a). We calculated instantaneous theta frequency, amplitude and phase using a Hilbert transform. In periods where running speed was greater than 5 cm/s, the slope and intercept of theta frequency with respect to running speed were calculated using least-squares linear regression. Slopes and intercepts of linear fits were compared between baseline, gain decrease and gain increase (Supplementary Fig. 11b). Slope changes were converted into an angle that varied between 0 and 90°, with full locomotor weighting corresponding to an angle of 45° and full visual weighting corresponding to arctan(0.5), or 26.6°, in gain decrease and arctan(1.5), or 56.3°, in gain increase (Supplementary Fig. 11c). These angles were then converted into percentage weights of visual versus locomotor cues (Supplementary Fig. 11c).

Pairs of grid and speed cells. To analyze correlations between grid and speed cells, we identified all pairs of recorded units in which one was a grid cell and the other was a speed cell (Supplementary Fig. 14a). Conjunctive grid × speed cells were also included in this analysis. Recordings from the same pair in different sessions were treated as separate data points (26 grid cells, 17 speed cells and 11 conjunctive grid × speed, 58 unique grid–speed pairs). We computed the percent weighting of visual cues based on the change in speed cell slope (Fig. 4) and the change in field size (Supplementary Fig. 6c,d) and correlated these metrics across pairs (Supplementary Fig. 14b). We then averaged speed slopes and field sizes by session, recomputed visual weights, and computed correlations across sessions in which both speed and grid cells were recorded (Supplementary Fig. 14c).

Optic flow track. During optic flow experiments (Supplementary Fig. 16), mice ran on a 400-cm track with black and white bars on the walls (spatial period = 13 cm) but no visual landmarks along the length of the track. On the optic flow track, average angular velocities of the visual cues during peak running speeds ranged from 0° s⁻¹ straight ahead to 240° s⁻¹ at 90 degrees to the mouse. These values are well within the range at which visual cortex neurons respond to moving bars[40]. Grid cells drifted slowly on the cue-rich track, as in previous observations of grid cells in VR[53] (Supplementary Fig. 16a). As this led to lower whole-session stability on the cue-rich track, we examined trial-to-trial stability as follows (Supplementary Fig. 16b,c). First, single-trial firing rate vectors were created by smoothing the vector of spike counts in each spatial bin for each trial with a Gaussian kernel (s.d. = 5 cm). We then calculated the Pearson correlation between single-trial firing rate vectors in every pair of adjacent trials and averaged over trials. A sliding window analysis was used to measure the stability of the firing rate maps as a function of position on the track. Firing rate maps were computed separately for the first and second half of the session. We then calculated Pearson's correlation between the firing rate in the first and second half of the session in a 50-cm window that was moved across the track in increments of 1 bin. To assess the response of speed cells, we compared cells that passed the speed cell criteria on the cue-rich track to cells that passed on the optic flow track (Supplementary Fig. 16d).

Reporting Summary. Further information on experimental design is available in the Nature Research Reporting Summary linked to this article.

Code availability. Custom MATLAB scripts used to analyze the data are available upon reasonable request.

Data availability. All data are available from the authors upon reasonable request.

References

47. Giocomo, L. M. et al. Grid cells use HCN1 channels for spatial scaling. *Cell* **147**, 1159–1170 (2011).
48. Kadir, S. N., Goodman, D. F. & Harris, K. D. High-dimensional cluster analysis with the masked EM algorithm. *Neural Comput.* **26**, 2379–2394 (2014).
49. Franklin, K.B.J. & Paxinos, G. *The Mouse Brain in Stereotaxic Coordinates* 3rd edn. (Academic, London, 2007).
50. Langston, R. F. et al. Development of the spatial representation system in the rat. *Science* **328**, 1576–1580 (2010).
51. Wills, T. J., Cacucci, F., Burgess, N. & O'Keefe, J. Development of the hippocampal cognitive map in preweanling rats. *Science* **328**, 1573–1576 (2010).
52. Domnisoru, C., Kinkhabwala, A. A. & Tank, D. W. Membrane potential dynamics of grid cells. *Nature* **495**, 199–204 (2013).
53. Yoon, K., Lewallen, S., Kinkhabwala, A. A., Tank, D. W. & Fiete, I. R. Grid cell responses in 1D environments assessed as slices through a 2D lattice. *Neuron* **89**, 1086–1099 (2016).

natureresearch

Corresponding author(s): Lisa M Giocomo, Malcolm G Campbell

Reporting Summary

Nature Research wishes to improve the reproducibility of the work that we publish. This form provides structure for consistency and transparency in reporting. For further information on Nature Research policies, see Authors & Referees and the Editorial Policy Checklist.

Statistical parameters

When statistical analyses are reported, confirm that the following items are present in the relevant location (e.g. figure legend, table legend, main text, or Methods section).

n/a	Confirmed	
☐	☒	The exact sample size (*n*) for each experimental group/condition, given as a discrete number and unit of measurement
☐	☒	An indication of whether measurements were taken from distinct samples or whether the same sample was measured repeatedly
☐	☒	The statistical test(s) used AND whether they are one- or two-sided *Only common tests should be described solely by name; describe more complex techniques in the Methods section.*
☐	☒	A description of all covariates tested
☐	☒	A description of any assumptions or corrections, such as tests of normality and adjustment for multiple comparisons
☐	☒	A full description of the statistics including central tendency (e.g. means) or other basic estimates (e.g. regression coefficient) AND variation (e.g. standard deviation) or associated estimates of uncertainty (e.g. confidence intervals)
☐	☒	For null hypothesis testing, the test statistic (e.g. *F*, *t*, *r*) with confidence intervals, effect sizes, degrees of freedom and *P* value noted *Give P values as exact values whenever suitable.*
☒	☐	For Bayesian analysis, information on the choice of priors and Markov chain Monte Carlo settings
☒	☐	For hierarchical and complex designs, identification of the appropriate level for tests and full reporting of outcomes
☐	☒	Estimates of effect sizes (e.g. Cohen's *d*, Pearson's *r*), indicating how they were calculated
☐	☒	Clearly defined error bars *State explicitly what error bars represent (e.g. SD, SE, CI)*

Our web collection on statistics for biologists may be useful.

Software and code

Policy information about availability of computer code

Data collection	Electrophysiological data were collected using Axona's DacqUSB software. Behavioral data was collected from virtual reality environments programmed in Unity. Ball rotation was read using custom Arduino code.
Data analysis	Analyses were carried out using MATLAB scripts. MATLAB was used to perform statistical calculations. Cell clusters were isolated using Axona's TINT cluster-cutting software.

For manuscripts utilizing custom algorithms or software that are central to the research but not yet described in published literature, software must be made available to editors/reviewers upon request. We strongly encourage code deposition in a community repository (e.g. GitHub). See the Nature Research guidelines for submitting code & software for further information.

Data

Policy information about availability of data

All manuscripts must include a data availability statement. This statement should provide the following information, where applicable:
- Accession codes, unique identifiers, or web links for publicly available datasets
- A list of figures that have associated raw data
- A description of any restrictions on data availability

All data are available upon reasonable request.

Field-specific reporting

Please select the best fit for your research. If you are not sure, read the appropriate sections before making your selection.

☒ Life sciences ☐ Behavioural & social sciences ☐ Ecological, evolutionary & environmental sciences

For a reference copy of the document with all sections, see nature.com/authors/policies/ReportingSummary-flat.pdf

Life sciences study design

All studies must disclose on these points even when the disclosure is negative.

Sample size	Sample sizes were based upon on convention in the field. At least 28 cells of each type (grid, border, speed) were collected for each comparison in the main figures.
Data exclusions	Cells with low firing rates (< 100 spikes in open field, < 0.2 Hz in VR) and sessions with low coverage (< 70%) were excluded. Grid and border cells that did not pass our quantitatively defined stability thresholds were not included in structural analyses, as described in the results section of the manuscript. In theta analyses (Supplementary Fig. 11), only mice with at least 3 sessions with significant theta power were included (17/20 mice). Data from mouse 21 was only included in Figure 6 as it was collected for this purpose during the revision process.
Replication	Over the course of revising this manuscript, results have been reliably reproduced in new data that have been added.
Randomization	Randomization is not applicable to experimental groups, as mice typically experienced a combination of baseline, gain increase and gain decrease sessions. For the path integration task, trials in which gain was altered were randomized, as were trials in which the reward was omitted. This randomization process was applied to all mice included in the behavioral study.
Blinding	Experimenters were not blinded, as there were not separated groups in this study.

Reporting for specific materials, systems and methods

Materials & experimental systems

n/a	Involved in the study
☒	Unique biological materials
☒	Antibodies
☒	Eukaryotic cell lines
☒	Palaeontology
☐	☒ Animals and other organisms
☒	Human research participants

Methods

n/a	Involved in the study
☒	ChIP-seq
☒	Flow cytometry
☒	MRI-based neuroimaging

Animals and other organisms

Policy information about studies involving animals; ARRIVE guidelines recommended for reporting animal research

Laboratory animals	Mice were C57BL/6 aged 6 weeks to 6 months. Both male and female mice were used.
Wild animals	No wild animals were used in this study.
Field-collected samples	No field-collected samples were used in this study.